Advanced Nanofabrication of Thermal Emission Devices

by

Fergus Hurley

B.E. Electrical and Electronic Engineering
University College Cork, Ireland 2006

Submitted to the Department of Electrical Engineering and Computer Science
in partial fulfillment of the requirements for the degree of

Master of Science in Electrical Engineering

at the

MASSACHUSETTS INSTITUTE OF TECHNOLOGY

May 2008
[June 2008]

Signature of Author _____

Fergus Hurley
Department of Electrical Engineering and Computer Science
May 23, 2008

Certified by_

John G. Kassakian
Professor of Electrical Engineering and Computer Science
Thesis Supervisor
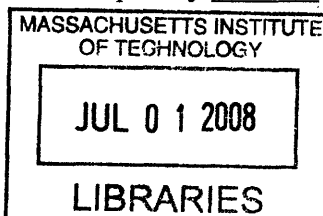
Certified by_

Ivan Čelanović
Post Doctoral Researcher
Thesis Co-Supervisor

Accepted by _____

Terry P. Orlando
Professor of Electrical Engineering and Computer Science
Chair, Department Committee on Graduate Students

Advanced Nanofabrication of Thermal Emission Devices

by

Fergus Hurley

Submitted to the Department of Electrical Engineering and Computer Science
on May 23, 2008, in partial fulfillment of the
requirements for the degree of
Master of Science

Abstract

Nanofabricated thermal emission devices can be used to modify and modulate blackbody thermal radiation. There are many areas in which altering thermal radiation is extremely useful, especially in static power conversion, lighting and sensor applications. Two specific thermal emission devices which show great promise include resonant thermal emitters and selective thermal emitters. It has been found from theory that resonant thermal emitters exhibit quasi-monochromatic and partially coherent thermal emission when fabricated with a 2-dimensional photonic crystal structure in a high-dielectric low-absorption material such as silicon. This type of fabricated resonant thermal emitter has great potential for use as near-IR and IR sensors. Theory has also shown that selective thermal emitters fabricated in tungsten with a 2-dimensional photonic crystal structure can exhibit spectrally selective thermal emission. This type of fabricated selective thermal emitter can be used to increase the efficiency of thermophotovoltaic (TPV) systems by preventing the incident thermal radiation below the band-gap of the PV diode from reaching the PV diode.

This thesis explores the nanofabrication of a 2-dimensional photonic crystal silicon-on-sapphire (SOS) resonant thermal emitter which is now possible to fabricate due to advances in fabrication technology. Initially, the theory behind the SOS resonant thermal emitter which exhibits multiple resonant emission peaks is discussed. Next, an in-depth examination of the theory behind the technology used in the fabrication the resonant thermal emitter is investigated. Then, the SOS resonant thermal emitter fabrication process and characterization which was performed is discussed. The results showed that it was possible to fabricate the required 2-dimensional pattern but that there were issues with the pattern transfer into silicon, which needs to be further researched.

Thesis Supervisor: John G. Kassakian
Title: Professor of Electrical Engineering and Computer Science

Thesis Co-Supervisor: Ivan Čelanović
Title: Post Doctoral Researcher at the Laboratory for Electromagnetic and Electronic Systems

Acknowledgments

I would like to express my deepest gratitude to all the people with whom I have had the immense pleasure to study, teach and perform research with at MIT. In particular I wish to thank Professor John G. Kassakian, my supervisor for the opportunities he has provided me with and the support, encouragement and guidance he has offered me in my research and throughout my time at MIT. JGK truly is a legend.

I am very grateful to Dr. Ivan Čelanović, my co-supervisor for believing in me and providing me with the opportunity to work in the area of nanofabrication of thermal emission devices. His encouragement and supervision has been a great asset and I have learnt an extraordinary amount from him about how to approach research problems. It has been a great privilege to work with such a fantastic researcher.

I would like to thank Natalija Jovanovic for helping me become established in the fab and for devoting time to supervising my day to day activities at the outset of my research. Her unique ability to instill motivation in me and assistance in digging deeper on the fabrication aspects of my research was invaluable.

My appreciation goes to all the staff and students in the Nanostructures Laboratory, the Technology Research Laboratory and the Exploratory Materials Laboratory at MIT. I am particularly grateful to Kurt Broderick, Jim Daley, Tim Savas and Donal Jamieson for all their help and guidance on the intricacies of fabrication. I would also like to thank all the administrators in the Laboratory for Electromagnetic and Electronic Systems and in the Department of Electrical Engineering and Computer Science for taking care of all the formalities.

I am grateful to all the students in the Laboratory for Electromagnetic and Electronic Systems for treating me with respect and helping me feel at home during my time in the lab. I would like to give a special thanks to all the inspirational characters that I have had the pleasure of becoming friends with through my involvement in EECS classes, the MIT Energy Cub and as residential advisor for the No.6 Club fraternity house.

Lastly, and most importantly, I wish to thank my family, whose love and support made this and everything else in my life possible and to whom I owe everything. You're the best!

Contents

Contents

List of Figures

List of Tables

This chapter provides context for the research into the nanofabrication of thermal emission devices presented in this thesis. The first section explains the motivation behind this research. It introduces some of the relevant literature on the theory behind and fabrication of the thermal emission device investigated in this research, the 2-dimensional silicon-on-sapphire (SOS) resonant thermal emitter. It also discusses some results which have been achieved in fabricating similar structures. The second section gives an overview of the content of each chapter in this thesis.

1.1   Thesis Motivation

It has only recently become possible, due to advances in the semiconductor processing technology, to fabricate structures on the order of the wavelength of light. This has created the potential for exciting research in areas other than just the semiconductor industry. One such area is the use of photonic crystals in thermal emission devices to modify and modulate black body thermal radiation. Theory has shown that it is possible to create a resonant thermal emitter using a 2-dimensional photonic crystal in a high-dielectric low-absorption material which exhibits quasi-monochromatic and partially coherent thermal emission [1], [2]. It has also been shown from theory that it is possible to create a selective thermal emitter which exhibits broadband thermal emission by using a similar structure photonic crystal to the resonant thermal emitter but fabri-

cated in a metalic material and which can be used in thermophotovoltaic systems to increase efficiency [1].

The objective of this thesis is to develop, characterize and implement a new nanofabrication process for a 2-dimensional photonic crystal SOS resonant thermal emitter. Such a resonant thermal emitter could be used in many applications such as a near-IR or IR sources and detectors. The fabrication procedure for the 2-dimensional photonic crystal SOS resonant thermal emitter is quite similar to that of the 2-dimensional photonic crystal tungsten selective thermal emitter. Research has already been performed into the fabrication of the later [3]. However, the fabrication of the 2-dimensional SOS resonant thermal emitter involves using different materials and increasing the complexity of the fabrication procedure with the potential for improved dimensional control, a key parameter for fabricating high-Q resonant thermal emitters, and so the results of this thesis could be used to improve the 2-dimensional photonic crystal tungsten selective thermal emitter fabrication and consequently the TPV system performance.

1.2   Thesis Outline

The next chapter, Chapter 2, introduces photonic crystals and discusses two specific thermal emission devices, a resonant thermal emitter and a selective thermal emitter, which both use a similar 2-dimensional photonic crystal structure. Chapter 3 analyzes the main fabrication technologies which can be used to create the desired 2-dimensional photonic crystal structure in silicon for the resonant thermal emitter. Chapter 4 discusses the three main stages in the fabrication of the 2-dimensional photonic crystal SOS resonant thermal emitter. The three main stages include

deposition, lithography and etching and each consists of many individual steps. The implementation, characterization and results of each of these steps are also discussed. The final chapter, Chapter 5, summarizes the work which has been presented in this thesis and offers some suggestion of future avenues for research.

Chapter 2

Thermal Emission Devices

This chapter introduces photonic crystals and discusses the application of photonic crystals to two thermal emission devices. The two thermal emission devices are a resonant thermal emitter and a selective thermal emitter. Both of these emitters can be formed using geometrically similar 2-dimensional photonic crystal structure. The rest of the thesis continues with the fabrication of the resonant thermal emitter.

2.1   Photonic Crystals

Photonic crystals possess the unique ability to control and manipulate the generation, absorption and propagation of electromagnetic waves [4]. They consist of periodically varying refractive indices which can be oriented to form 1-dimensional, 2-dimensional or 3-dimensional structures, Fig. 2.1. By changing the geometrical properties of the material it is possible to form metamaterials with tailored optical properties.
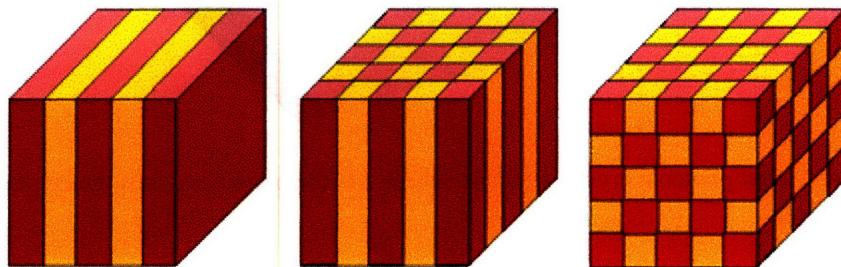
Figure 2.1: Illustration of a 1-, 2- and 3-dimensional photonic crystal. Adapted from [5].

Numerous examples of photonic crystals occur in nature, such as in opal gemstones and Morpho butterflies, but it has only recently become possible to fabricate photonic crystals [6]. There are several different geometries and applications of photonic crystals. This thesis focuses on the fabrication of a 2-dimensional photonic crystal geometry. An application of such a geometry is as a resonant thermal emitter which requires fabricating a silicon-on-sapphire (SOS) 2-dimensional photonic crystal structure. Another application is as a selective thermal emitter which requires fabricating a tungsten 2-dimensional photonic crystal structure. Figure 2.2 illustrates a similar 2-dimensional photonic crystal structure to the one used to fabricate the resonant thermal emitter and selective thermal emitter. The periodicity, depth and diameter of the holes can be adjusted to achieve the desired electromagnetic wave propagation in the infrared region of the spectrum.
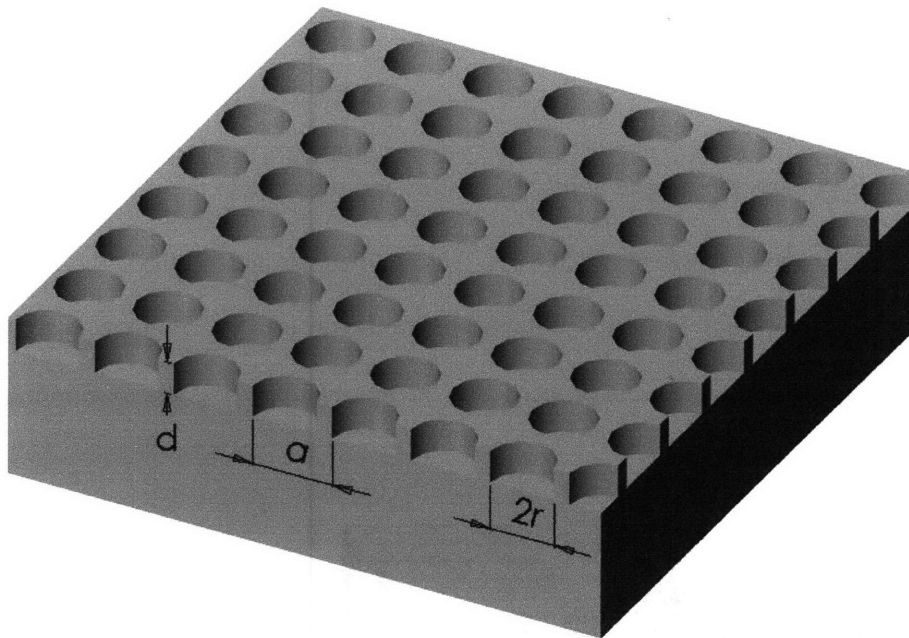
Figure 2.2: 2-dimensional photonic crystal structure where *a* is the periodicity, *d* is the depth and *2r* is the diameter of the holes.

2.2   Resonant Thermal Emitter

Through theory and simulation it has been shown that a 2-dimensional photonic crystal silicon slab exhibits narrow-band thermal emission peaks in the infrared region of the spectrum [1], [2]. The hole radius and free electron absorption can be adjusted to match the desired resonant frequency. Simulation of a 2-dimensional photonic crystal with a periodic square lattice of spatial period a and holes of radius r where $r = 0.15a$ have exhibited several resonant peaks as shown in Fig. 2.3 [1], the structure of which is shown in Fig. 2.4. An equal amount of photons are emitted from the top side and bottom, sapphire, side of the 2-dimensional silicon on sapphire photonic crystal. Therefore it must be noted that the value of emittance shown in Fig. 2.3 is for only one side. There are many possible applications where it would be useful to be able to switch on or off the emission of radiation by simply changing the temperature of a substrate, including IR sensing, detection (enhanced bolometer) and light generation. This thesis focused on the development of a fabrication process for this novel structure.
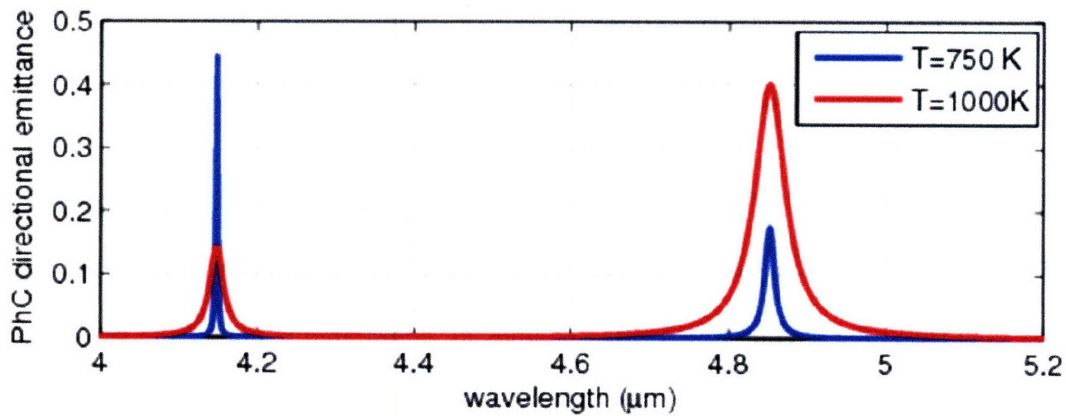
Figure 2.3: Simulated 2-dimensional silicon photonic crystal slab with 1 μm periodicity and 400 nm diameter holes displaying anomalous emittance (non-blackbody) and thermal radiation intensity at 750 K and 1000 K. Adapted from [1].
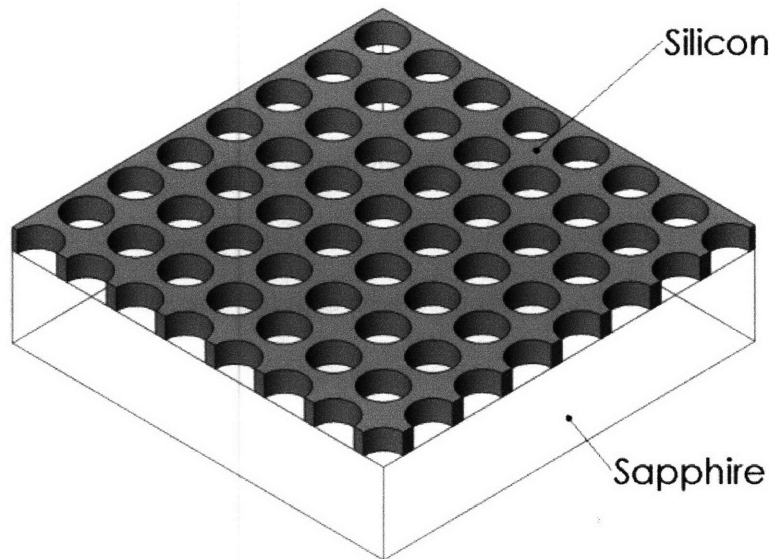
Figure 2.4: Resonant thermal emitter 2-dimensional silicon-on-sapphire photonic crystal structure.

2.3   Selective Thermal Emitter

A thermophotovoltaic converter is a static energy conversion device that converts heat into photons and then into electricity. The idea of a TPV system was first proposed at MIT around 1956 [7], [8]. It is only now becoming possible, due to advances in material science and fabrication techniques, for TPV systems to reach an efficiency which is competitive in certain applications with other electrical energy conversion devices.

In a basic TPV system there are three main components, a high temperature source, an emitter and a photovoltaic (PV) diode. The high temperature source is in the range of 1000 - 2000 K and is directly coupled to the emitter which emits photons in the infrared region of the spectrum. A photovoltaic diode converts incident photons above a certain minimum energy level, the band-gap energy, into electricity. Currently, due to economic reasons, gallium antimonide (GaSb) is the PV diode of choice in most TPV systems. GaSb has a band-gap of 0.78 eV which is less than that

of silicon, 1.12 eV, but still only converts a relatively small amount of the radiated spectrum, wavelengths shorter than 1.7 µm, into electricity. To increase the efficiency of the GaSb PV diode a selective thermal emitter is used to supress radiation below the band-gap, wavelengths longer than 1.7 µm, from reaching the PV diode. A selective thermal emitter which offers the possibility of significantly improving TPV efficiency is the 2-dimensional tungsten photonic crystal structure, the emittance and structure of which is shown in Fig. 2.5 [1] and Fig. 2.6 respectively. The reason for the difference between the emittance of the two structures is that the cavities in the selective thermal emitter rely on multiple resonances with relatively low Q factor to enhance broadband emission whereas the cavities in the resonant thermal emitter rely on isolated resonances to enhance narrow band emission. As mentioned previously, this structure has already been fabricated but based on the fabrication process developed in this thesis there is potential to achieve improved dimensional control and uniformity in the fabrication method of the selective thermal emitter which has the potential of increased TPV performance.
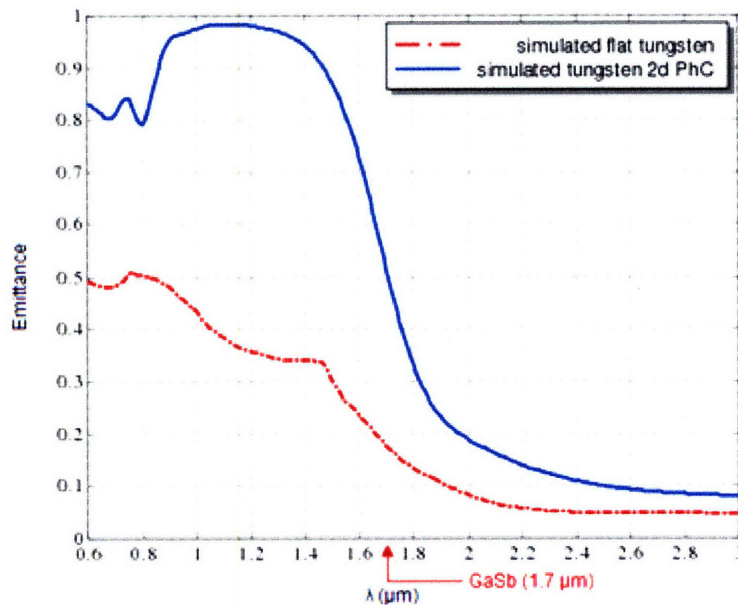
Figure 2.5: Simulated normal emittance of flat tungsten and a 2-dimensional tungsten photonic crystal structure (1 µm periodicity, 800 nm hole diameter and infinite hole depth). Adapted from [1].
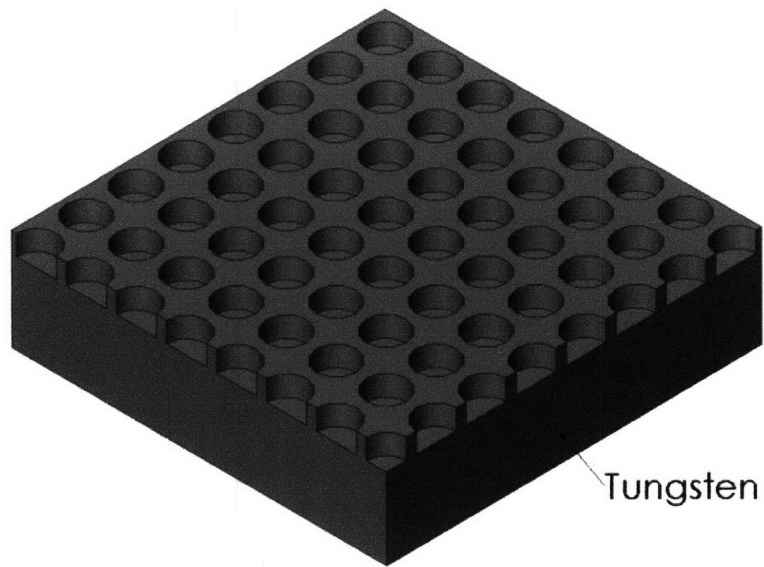
Figure 2.6: Selective thermal emitter 2-dimensional tungsten photonic crystal structure.

Resonant Thermal Emitter Fabrication Technology

The goal of this chapter is to describe the main technologies used in the fabrication of the resonant thermal emitter discussed in Chapter 2, specifically the 2-dimensional silicon-on-sapphire (SOS) photonic crystal structure. Chapter 4 then examines the specific materials, processes and parameters which were used to implement the fabrication technologies discussed in this chapter. The chapter consists of six sections, each of which gives an in-depth description of a specific fabrication technology which was used. The first section examines chemical vapour deposition (CVD) which is used to deposit silicon dioxide on the surface of a substrate. Spin coating, another deposition technique, is examined in the second section and is used to coat the substrate with polymers of anti-reflection coating (ARC) and photoresist (PR). The third section discuses interference lithography which is used to form the desired grid pattern of holes in the PR. The next section analyzes the operation of ARC's which are used to prevent the unwanted exposure of the PR. The penultimate section investigates the characteristics of PR which is the photosensitive material used as the initial mask layer. Finally, the transfer of the pattern of holes from the PR into the other layers in the stack by reactive ion etching (RIE) is studied in section six. Most of the technologies discussed are commonly used in microfabrication and although all the technologies were used in this case to fabricate a resonant thermal emitter in SOS they could also be used to fabricate many other devices.

3.1   Chemical Vapor Deposition

CVD is a method of material synthesis in which the constituents of a vapor phase react to form a solid film at the surface of a substrate [11]. There are numerous different CVD techniques, most of which can be distinguished according to the form of energy that is supplied to chemically activate the process. The original technique developed was atmospheric pressure CVD (APCVD); in which film deposition takes place on substrates which are heated using an inductively coupled graphite susceptor at a pressure of 760 Torr. Plasma-enhanced CVD (PECVD) is a technique involving the application of sufficiently high voltages at low pressure, 10 mTorr – 10 Torr, to cause 'breakdown' of the gas and a glow discharge plasma, consisting of ions, electrons and electronically excited species, to appear and allows for low temperature deposition to take place [10]. PECVD has been used since the 1970's to deposit silicon nitride films for passivation layers to encapsulate integrated circuits and now is used to deposit thin films in the microfabrication of many devices such as transistors, photovoltaics and displays.

There are three fundamental stages of the PECVD process, as shown in Fig. 3.1. The first stage is the chemical activation of a gas molecule through electron impact causing dissociation into neutral radicals. This is achieved by an externally applied electrical field which causes plasma electrons, which are relatively light and easily accelerated, and ions, which are relatively heavy and therefore slower and less energetic. Due to the relatively large mass difference between the electrons and the gas molecules, low energy electrons do not lose much energy in collisions and collide elastically with the gas molecule. Therefore, plasma electrons accumulate energy in the electric field until an electron has enough energy so that an inelastic collision takes place. In an inelastic collision the electron loses energy to the gas molecule, which can electronically excite the

gas or cause it to dissociate or ionize. The energy required to cause ionization is much greater than that required for dissociation because the strong Coulombic forces to produce an ion and electron pair is much greater than that required to form two neutral fragments. Therefore, the density of ions in the plasma is much less than the density of radicals. Although only approximately one part per million of the gas consists of electrons and ions they sustain the most visible part of the process, the glow discharge.
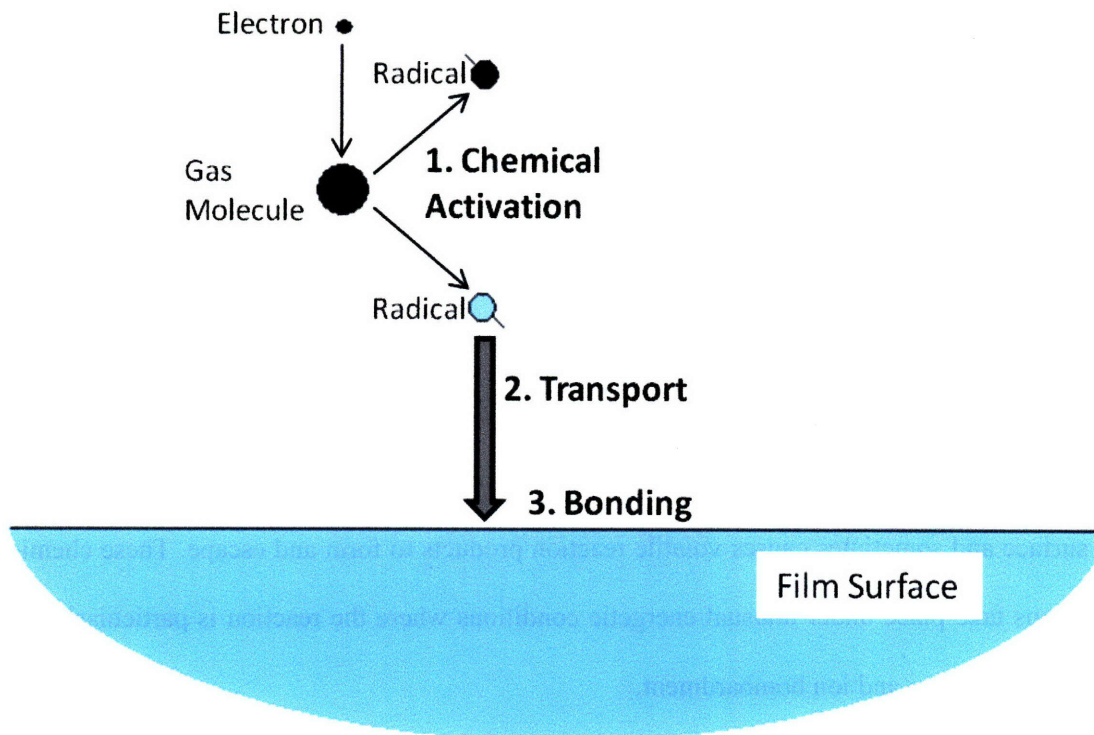
Figure 3.1: The three basic stages of the PECVD process: 1. chemical activation by electron impact, 2. transport of the activated species to the film surface and 3. bonding to the film surface.

The second stage in PECVD is the transport of the radical species to the substrate surface. In most PECVD systems the gas flow rates are so low that diffusion is the dominant transport mechanism of neutral radicals. Diffusion occurs mainly due to a concentration gradient between the radicals

generated in the plasma and their disappearance at the film surface. Radicals created in the plasma undergo many collisions before reaching the surface of the growing film. Most of the collisions are with the source gas, due to its abundance; when these collisions occur within one or two collisions there is an end to the chemical reaction between the radical and the gas, if there is a reaction at all. Although the probability of a radical colliding with another radical is small, the reaction product is usually reactive. If the process repeats, then the molecule continues to grow into a macromolecule, and then into a particle. The deposition of particles formed in the gas stream onto the surface of the film cause defects to occur in the film and determine to an important degree the properties of the film. However, it is possible to control the degree to which this undesirable process occurs by adjusting the variables of the PECVD system.

The third PECVD stage is the chemical reaction of the radicals arriving at the surface of the growing film. PECVD resembles plasma etching, explained in Section 3.6, differing mainly in the surface reaction outcome. In the case of plasma etching, the reaction produces volatile species that leave the surface. While in the case of PECVD, the reaction bonds at least part of the radical to the surface and sometimes causes volatile reaction products to form and escape. These chemical reactions take place under unusual energetic conditions where the reaction is particularly affected by temperature and ion bombardment.

In a PECVD system there are many variables which can be adjusted to change the properties of the film deposition, such as deposition temperature, chamber pressure, gas flow rates, input gas concentrations and the electrical power promoting the reaction. These primary process parameters enable an enormous parameter space of operation and make the PECVD system very versatile for thin film deposition.

3.2 Spin Coating

It is possible to form a thin uniform organic film of ARC and PR on a flat substrate by centrifugal spinning. An excess of the desired film material is applied as a fluid to the substrate and then rapidly rotated which causes the fluid to flow radially outwards and the excess fluid to spin off the edges of the substrate. As the fluid thins evaporation of volatile constituents takes place which causes the concentration to increase and a solid film results. The speed and duration of spinning can be varied to obtain very uniform films of desired thickness. Spin coating is commonly employed in the microfabrication of many devices, especially in the lithography stage, where an accurate thin uniform film with a thickness in the range of nanometers is required. There have been numerous studies performed on the spin coating process explaining the formation of the uniform film and the dependence of the formation on material parameters [12], [13], [14], [15].

Based on the two fundamental principles of fluid mechanics, conservation of mass and conservation of momentum, it is possible to derive an equation for the thickness of a thin film formed by spin coating. First considering the conservation of mass, the continuity equation for fluid dynamics states that in steady state the rate at which mass enters a system is equal to the rate at which mass leaves. The continuity equation for a single-phase fluid is

$$\frac{\partial \rho}{\partial t} + \nabla \cdot \rho v = 0 \tag{3.1}$$

where ρ is the fluid density, t is the total spinning time and v is the velocity vector. The divergence of the velocity vector can be expressed in 3-dimensional cylindrical coordinates (r, θ, z)

$$\nabla \cdot \boldsymbol{v} = \frac{1}{r}\frac{\partial}{\partial r}(rv_r) + \frac{1}{r}\frac{\partial v_\theta}{\partial \theta} + \frac{\partial v_z}{\partial z} = 0 \qquad (3.2)$$

Therefore the continuity equation in cylindrical coordinates (r, θ, z) is

$$\frac{\partial \rho}{\partial t} + \frac{1}{r}\frac{\partial}{\partial r}(\rho r v_r) + \frac{1}{r}\frac{\partial}{\partial \theta}(\rho v_\theta) + \frac{\partial}{\partial z}(\rho v_z) = 0 \qquad (3.3)$$

Second, the conservation of momentum, a form of Newton's second law, for a continuous fluid relates the velocities, pressure and stresses and is given by

$$\rho\left(\frac{\partial \boldsymbol{v}}{\partial t} + \boldsymbol{v}\cdot\nabla\boldsymbol{v}\right) = -\nabla p + \nabla\cdot\boldsymbol{\tau} + \rho f \qquad (3.4)$$

The terms on the left hand side of (3.4) result from the inertia of the fluid where the term $\frac{\partial \boldsymbol{v}}{\partial t}$ comes from the unsteady acceleration while the $\boldsymbol{v}\cdot\nabla\boldsymbol{v}$ term comes from the convective acceleration. The f term represents the body force which result mostly from gravity, g, but in certain applications takes into account other forces such as electromagnetic. The ∇p and $\nabla\cdot\boldsymbol{\tau}$ terms represent the stresses in the fluid where ∇p describes the pressure gradient and $\nabla\cdot\boldsymbol{\tau}$ represents the viscous forces. Assuming that the fluid is Newtonian and incompressible then it is possible to state that $\boldsymbol{\tau}$, a stress tensor, is given by

$$\tau = \mu\Delta \qquad (3.5)$$

where Δ is the rate of deformation tensor which in the case of a Newtonian fluid is assumed to be independent of the μ. Substituting (3.5) into (3.4) gives the equation of motion for a Newtonian fluid, which in vector representation is

$$\rho\left(\frac{\partial \boldsymbol{v}}{\partial t} + \boldsymbol{v} \cdot \nabla \boldsymbol{v}\right) = -\nabla p + \mu \nabla^2 \boldsymbol{v} + \rho \boldsymbol{f} \tag{3.6}$$

This is known as Navier-Stokes equation for a Newtonian and incompressible fluid. It can also be stated in terms of cylindrical coordinates as

r component:

$$\rho\left(\frac{\partial v_r}{\partial t} + v_r \frac{\partial v_r}{\partial r} + \frac{v_\theta}{r}\frac{\partial v_r}{\partial \theta} - \frac{v_\theta^2}{r} + v_z \frac{\partial v_r}{\partial z}\right)$$
$$= -\frac{\partial p}{\partial r} + \mu\left\{\frac{\partial}{\partial r}\left[\frac{1}{r}\frac{\partial}{\partial r}(rv_r)\right] + \frac{1}{r^2}\frac{\partial^2 v_r}{\partial \theta^2} - \frac{2}{r^2}\frac{\partial v_\theta}{\partial \theta} + \frac{\partial^2 v_r}{\partial z^2}\right\} + \rho g_r \tag{3.7}$$

θ component:

$$\rho\left(\frac{\partial v_\theta}{\partial t} + v_r \frac{\partial v_\theta}{\partial r} + \frac{v_\theta}{r}\frac{\partial v_\theta}{\partial \theta} + \frac{v_r v_\theta}{r} + v_z \frac{\partial v_\theta}{\partial z}\right)$$
$$= -\frac{1}{r}\frac{\partial p}{\partial \theta} + \mu\left\{\frac{\partial}{\partial r}\left[\frac{1}{r}\frac{\partial}{\partial r}(rv_\theta)\right] + \frac{1}{r^2}\frac{\partial^2 v_\theta}{\partial \theta^2} + \frac{2}{r^2}\frac{\partial v_r}{\partial \theta} + \frac{\partial^2 v_\theta}{\partial z^2}\right\} + \rho g_\theta \tag{3.8}$$

z component:

$$\rho\left(\frac{\partial v_z}{\partial t} + v_r \frac{\partial v_z}{\partial r} + \frac{v_\theta}{r}\frac{\partial v_z}{\partial \theta} + v_z \frac{\partial v_z}{\partial z}\right)$$
$$= -\frac{\partial p}{\partial z} + \mu\left\{\frac{1}{r}\frac{\partial}{\partial r}\left(r\frac{\partial v_z}{\partial r}\right) + \frac{1}{r^2}\frac{\partial^2 v_z}{\partial \theta^2} + \frac{\partial^2 v_z}{\partial z^2}\right\} + \rho g_z \tag{3.9}$$
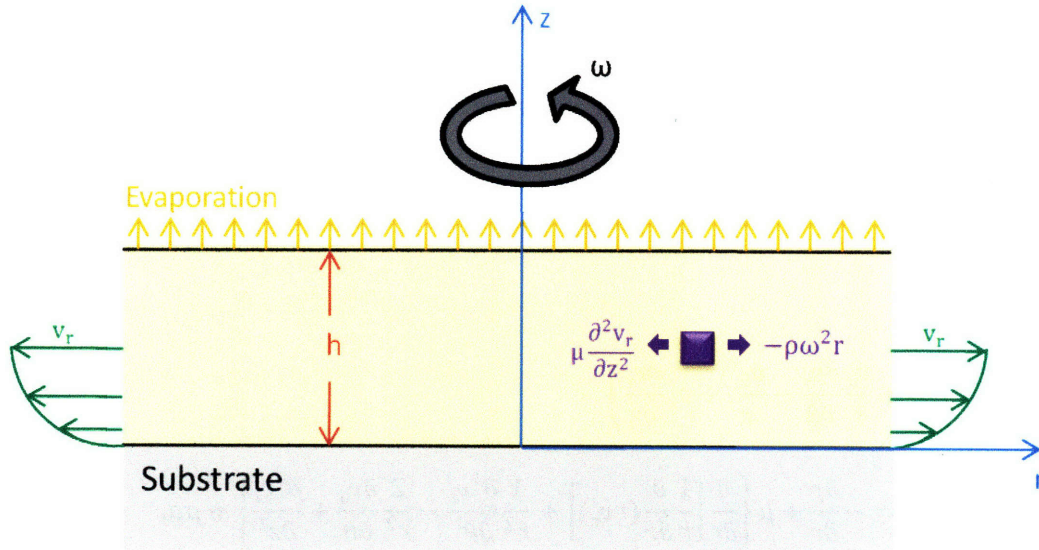
Figure 3.2: Illustration of the spin coating process.

In the case of spin coating, Fig. 3.2 shows the coordinate system and variables of interest. Based on this coordinate system it is possible to make a number of assumptions to simplify the application of Navier-Stokes equation to spin coating. Beginning with the following assumptions:

1. Axially symmetric laminar flow takes place.

2. The radial velocity dominates, $v_r \gg v_z$.

3. Quasi-steady state has been reached so the velocity gradient, $\frac{\partial v_r}{\partial t}$ in (3.7), can be neglected.

4. The shear stress arising from the velocity gradient is much larger than the stresses arising from the variation of v_r in the radial direction so the terms $\rho v_r \frac{\partial v_r}{\partial r}$ and $\mu \frac{\partial}{\partial r}\left[\frac{1}{r}\frac{\partial}{\partial r}(r v_r)\right]$ in (3.7) can be disregarded.

5. The equilibrium between the centrifugal term, $-\frac{\rho v_\theta^2}{r}$, and the viscous resistance, $\mu \frac{\partial^2 v_r}{\partial z^2}$, in (3.9) causes a steady flow to be achieved. Based on the previous assumptions and the fact that v_z is small, all the other terms in the equation can be neglected,

6. There is no radial gravitational component because the plane is horizontal.

7. The liquid layer is so thin that differences in gravitational potential have negligible effects in distributing the liquid compared with the effect of centrifugal forces and v_z is assumed to be small so (3.9) reduces to $0 = -\frac{\partial p}{\partial z}$.

8. The pressure distribution external to the film is uniform.

9. The impact of surface tension is insignificant.

The above assumptions allow the Navier-Stokes equations in cylindrical coordinates to be reduced to

$$\frac{-\rho v_\theta^2}{r} = \mu \frac{\partial^2 v_r}{\partial z^2} - \rho \frac{\partial p}{\partial r} \tag{3.10}$$

and

$$0 = -\frac{\partial p}{\partial z} \tag{3.11}$$

Based on assumptions 2 and 9, it is valid to assume that pressure is the only stress exerted in the z direction on the free surface and so the external pressure must be equal to the fluid pressure at the surface. It is shown by (3.11) that the pressure within the fluid is independent of z and based on assumption 8 the pressure is also independent of r. Therefore, the pressure is constant everywhere within the fluid and so (3.10) reduces to

$$\frac{-\rho v_\theta{}^2}{r} = \mu \frac{\partial^2 v_r}{\partial z^2} \tag{3.12}$$

Assuming that the fluid moves as a rigid body in the θ direction at the same rotational speed as the substrate, given by $v_\theta = r\omega$, then (3.12) becomes

$$\mu \frac{\partial^2 v_r}{\partial z^2} = -\rho \omega^2 r \tag{3.13}$$

where ω is the rotational speed in radians per second.

In order to solve for the film thickness, $h = h(r,t)$, boundary conditions must be applied. At the substrate surface boundary with the fluid, $z = 0$, the fluid velocity is equal to that of the substrate and as there is no radial velocity in the solid so the first boundary condition is

$$v_r = 0 \qquad \text{at } z = 0 \tag{3.14}$$

The second boundary condition occurs at the surface of the fluid film, $z = h$, and relates to the shear stress balance where the shear stress in the fluid is

$$\tau = \mu \frac{\partial v_r}{\partial z} \tag{3.15}$$

Assuming that no shear stress is exerted on the fluid by the ambient gas, the second boundary condition is

$$\frac{\partial v_r}{\partial z} = 0 \qquad \text{at } z = h(r, t) \tag{3.16}$$

In order to solve for the film thickness, $h(r, t)$, an equation relating it to $v_r(z)$ is required. Based on the assumptions above the continuity equation, (3.3), becomes

$$\frac{1}{r}\frac{\partial}{\partial r}(rv_r) + \frac{\partial v_z}{\partial z} = 0 \tag{3.17}$$

Multiplying both sides of (3.17) by dz and integrating from 0 to h gives

$$\int_0^h \frac{1}{r}\frac{\partial}{\partial r}(rv_r)dz + \int_0^h \frac{\partial v_z}{\partial z}dz = 0 \tag{3.18}$$

It is possible to define the radial flow per unit length of circumference as

$$q = \int_0^h v_r\, dz \tag{3.19}$$

and the rate of change of thickness with time as

$$\frac{\partial h}{\partial t} = v_r|_{z=h} \tag{3.20}$$

Substituting (3.19) and (3.20) into (3.18) results in

$$\frac{1}{r}\frac{\partial}{\partial r}(rq) + \frac{\partial h}{\partial t} = 0 \tag{3.21}$$

Returning to (3.13), it is now possible to perform a double integral to obtain an expression v_r as

$$v_r = -\frac{1}{2\mu}\rho\omega^2 r z^2 - \frac{1}{\mu}\rho\omega^2 r h z \tag{3.22}$$

which means that

$$q = \int_0^h v_r\, dz = \frac{\rho\omega^2 r}{3\mu}h^3 \tag{3.23}$$

By substituting (3.23) into (3.21) the following differential equation is obtained

$$\frac{\partial h}{\partial t} = -\frac{1}{r}\frac{\partial}{\partial r}\left(\frac{\rho\omega^2}{3\mu}r^2 h^3\right) = -2\left(\frac{\rho\omega^2}{3\mu}\right)h^3 \tag{3.24}$$

After multiplying across by dt, diving across by h^3 and integrating both sides, the solution for the film thickness is obtained as

$$h(t) = \frac{h_0}{\sqrt{1 + 4\left(\frac{\rho\omega^2}{3\mu}\right)h_0^2 t}} \tag{3.25}$$

where the constant h_0, independent of r, corresponds to the initial height, $t = 0$, of the fluid layer.

Based on (3.25) a number of observations of how the film thickness varies can be made. First, it must be noted that the film gets thinner as the angular speed increases. Second, if the fluid thickness is initially uniform over the entire substrate then it remains uniform during spinning and independent of the size of the substrate. Third, the fluid layer decreases by 3 dB in a time

$$\tau = \frac{1}{4\left(\frac{\rho\omega^2}{3\mu}\right)h_0^2} \tag{3.26}$$

from which it can be observed that the thicker the initial layer, the faster the fluid thins out. Fourth, for very thin films, h<<h_0, the film thickness is independent of its initial condition,

$$h(t) = \sqrt{\left(\frac{3\mu}{4\rho}\right)}\frac{1}{\omega}\frac{1}{\sqrt{t}} \tag{3.27}$$

It must be noted that evaporation must occur in the spin coating process in order for a solid film to form and this fact has been ignored in the analysis. However, assuming that the concentration of the fluid is uniform then evaporation will occur over the entire surface area causing the solids concentration to increase uniformly.

3.3   Interference Lithography

Nanometer scale patterns of gratings and grids can be formed over a large area using a maskless lithography technique known as interference lithography (IL) [16]. The basic principle of IL is that two plane waves incident on a sample result in a standing wave pattern. This pattern is then imaged into a layer of photo sensitive material known as photoresist (PR).
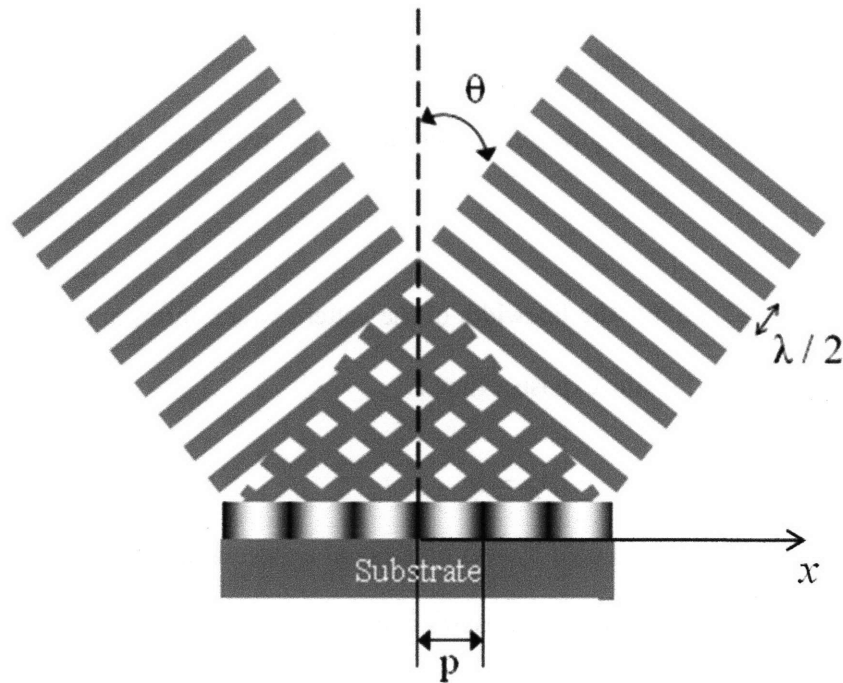
Figure 3.3: In interference lithography two plane waves interfere to form a pattern in photoresist. Adapted from [17].

The intensity of the standing wave pattern which result from the interaction of two plane waves of equal incident intensity is

$$I = 4I_0 sin^2 \left(\frac{\pi}{p} x \right) \tag{3.28}$$

where I is the total intensity, I_0 is the incident intensity from each plane wave, x is the position along the sample and p is the period of the of the standing wave pattern which is given by

$$p = \frac{\lambda}{2 sin(\theta)} \tag{3.29}$$

where λ is the wavelength of the incident waveform and θ is the angel of incidence [19]. It is possible to change the period of the standing wave pattern and thus the period of the pattern formed in the photoresist by changing the angle of incidence. However, the minimum period that can be achieved is $\frac{\lambda}{2}$ which is usually constant because the wavelength of the source is normally fixed.

The exposure dose, D_E, controls the linewidth of the pattern which forms and is obtained by the multiplying the intensity, I, by the exposure time t.

$$D_E = It \tag{3.30}$$

A 2-dimensional grid can be patterned by two orthogonal exposure doses, D_{E1} and D_{E2}. The pattern which forms as a result of the two exposures is given by the sum of the individual exposures doses

$$D_{ET} = D_{E1} + D_{E2} = 4I_{01} sin^2 \left(\frac{\pi}{p_1} x \right) t_1 + 4I_{02} sin^2 \left(\frac{\pi}{p_2} y \right) t_2 \tag{3.31}$$

where D_{ET} is the total exposure dose, I_{01} and I_{02} are the incident intensity from each plane wave during the first and second exposure respectively, t_1 and t_2 are the duration of the first and second exposures respectively, and p_1 and p_2 are the respective periods. In most practical cases the wavelength and incident irradiation are uncontrollable. However, an arbitrary grid pattern can

be created by adjusting the angel of incidence and the duration of each exposure resulting in different periods and linewidths respectively. In the case of a square grid pattern the periods and exposure times are set to be equal to each other for both exposures, $p_1 = p_2 = p$ and $t_1 = t_2 = t$, so (3.31) can be simplified to

$$D_{ET} = 4I_0 t \left(sin^2 \left(\frac{\pi}{p} x \right) + sin^2 \left(\frac{\pi}{p} y \right) \right) \tag{3.32}$$

Figure 3.4 shows the 2-dimensional standing wave pattern which results when the term in brackets in (3.32) is plotted, specifically the function $sin^2 \left(\frac{\pi}{p} x \right) + sin^2 \left(\frac{\pi}{p} y \right)$ is plotted for the case $p = 1$.
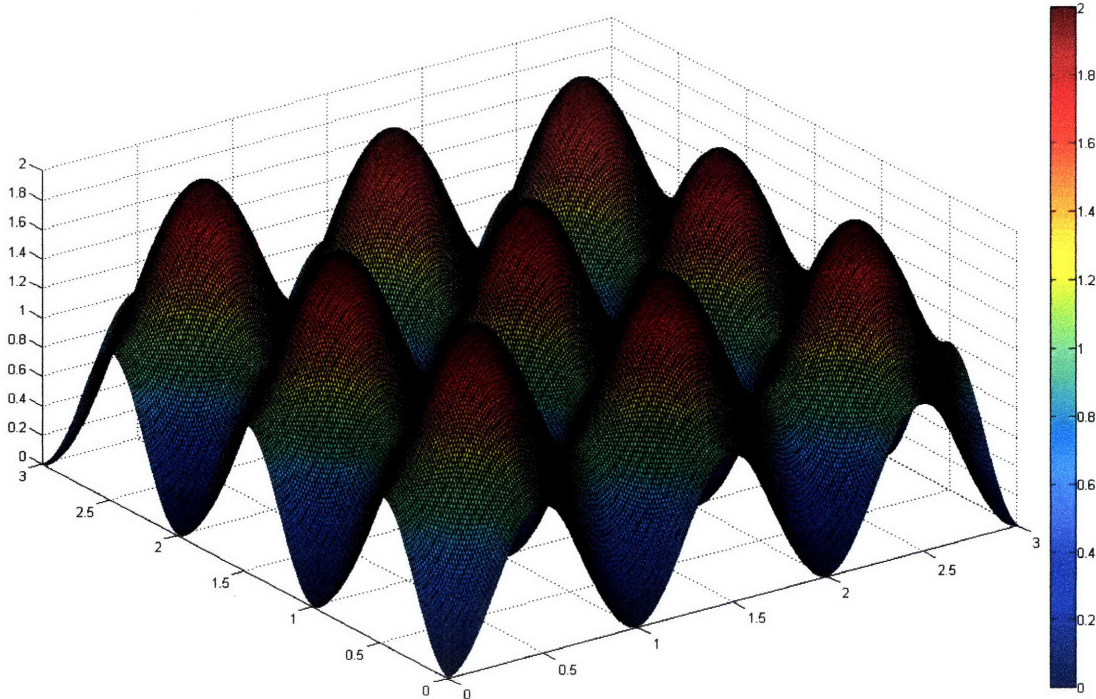
Figure 3.4: MATLAB plot of the function: $sin^2 (\pi x) + sin^2 (\pi y)$.

3.3.1 Pattern Formation

Patterns are formed in PR when part of the applied dose is greater than the clearing dose, D_C, which is the specific minimum value required to change the solubility of the PR. As the value of D_C is constant, in order to change the size of the patterned features the exposure time must be adjusted. PR's will be further examined in Section 3.5 but it is worth noting that there are basically two types of PR, negative and positive; in the case of negative resist the part which experiences a dose greater than D_C becomes insoluble in PR developer whereas the opposite occurs in positive PR.

As shown in the Section 3.3, the exposure dose for a square grid is given by (3.32). This equation proves that the exposure dose is proportional to the duration of the exposure and that it is spatially variable, as shown in Fig. 3.4. The shape of the feature is set by scaling the graph shown in Fig. 3.4 to represent the exposure dose and then taking a cross-section at D_C. In the case of a high-contrast negative resist, rods form when D_C is greater than 50% of the maximum value of the exposure dose whereas holes occur when the dose is less than 50% of the maximum value. Figure 3.5 shows the rods which result from a relatively small exposure dose. Figure 3.6 shows the square shaped holes which form when the D_C coincides with the saddle point of the exposure dose. The holes which form when the exposure dose is increased so that D_C occurs at 25% of the maximum value of the exposure dose is shown in Fig. 3.7. In the case of positive resist the inverse of these features would occur for the same conditions mentioned above.
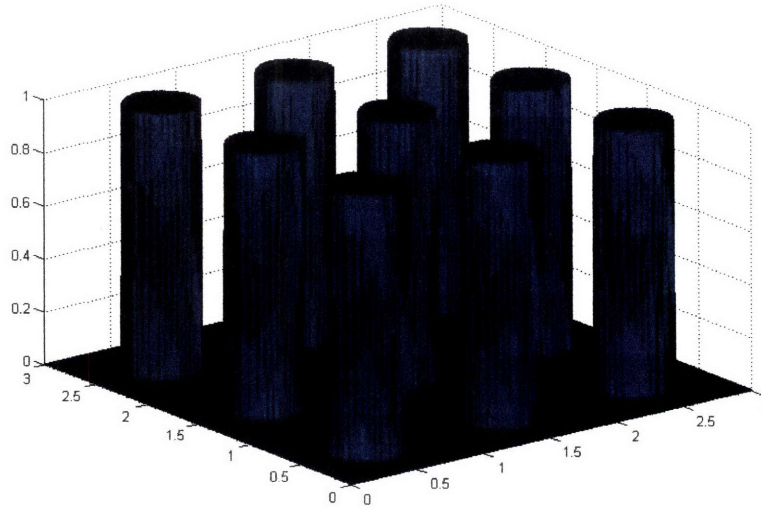
Figure 3.5: MATLAB plot of the rods which form in negative resist when the clearing dose occurs at 75% of the maximum value of the exposure dose.
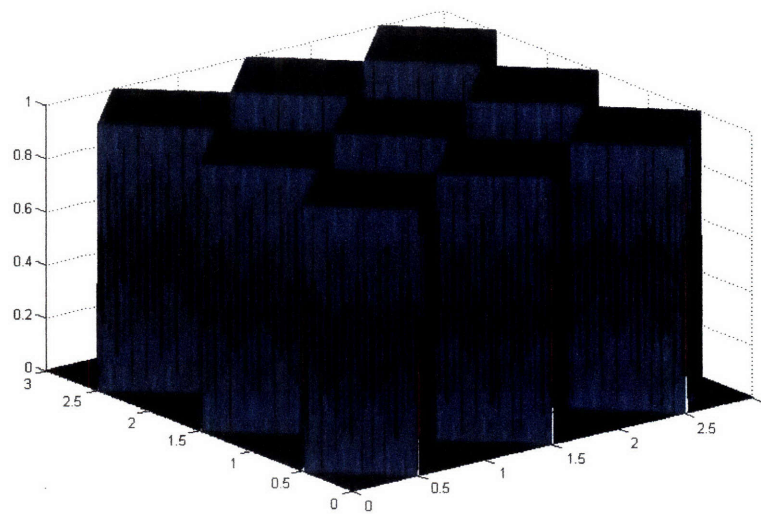
Figure 3.6: MATLAB plot of the square holes which form in negative resist when the clearing dose occurs at 50% of the maximum value of the exposure dose.
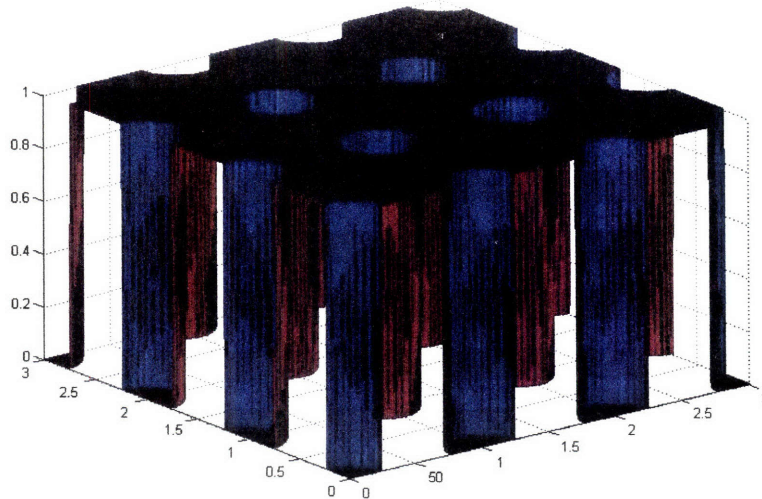
Figure 3.7: MATLAB plot of the holes which form in negative resist when the clearing dose occurs at 25% of the maximum value of the exposure dose.

3.3.2   Lloyd's Mirror Interference Lithography

There are various methods by which interference lithography can be implemented each of which has its own unique characteristics. One of the simplest methods is Lloyd's mirror IL which was developed in the nineteenth century and involves the use of a broad beam of light and a mirror to enable the reflection of part of the beam onto itself thus creating an interference pattern [16]. Figure 3.8 shows how in a Lloyd's mirror set-up some of the incident light is reflected off a mirror, which is at 90° to the substrate, resulting in two incident beams on the substrate with the same angle of incidence. As mentioned previously the angle of incidence, θ, of the beams is related to the period, p, of the interference pattern by

$$p = \frac{\lambda}{2sin(\theta)} \tag{3.33}$$

Therefore, by rotating the mirror/substrate assembly around the centre point it is possible to change the period of the pattern.
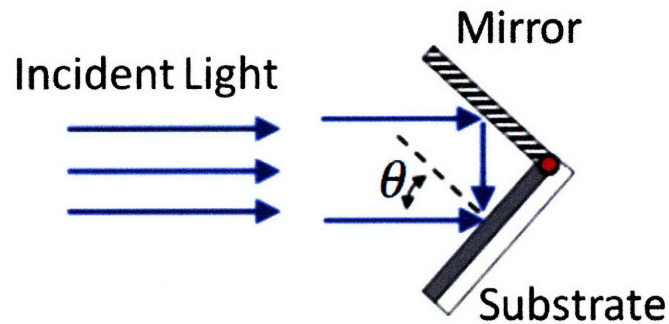
Figure 3.8: The essential components of a Lloyd's mirror set-up. Adapted from [17].

There are many advantages of the Lloyd's mirror IL system over other IL systems including ease of use and the fact that it is relatively inexpensive. Another advantage is it's insensitivity to vibrations due to the fact that the mirror is in physical contact with the sample and so there is just a single beam for most of the optical path. Another advantage is that precise alignment does not have to be performed in order to change the period of the pattern, the mirror/substrate assembly simply needs to be rotated. However, there are a few disadvantages of the Lloyd's mirror IL system which are primarily a result of the mirror. Dust particles and irregularities in the mirror surface result in scattering and phase variations of the reflected beam which reduces the linearity of the grating. Also, the difference in optical path length due to the fact that the light reflects off the mirror and the fact that the mirror can drift from being perfectly normal to the substrate results in reduced contrast between the interference fringes [20].
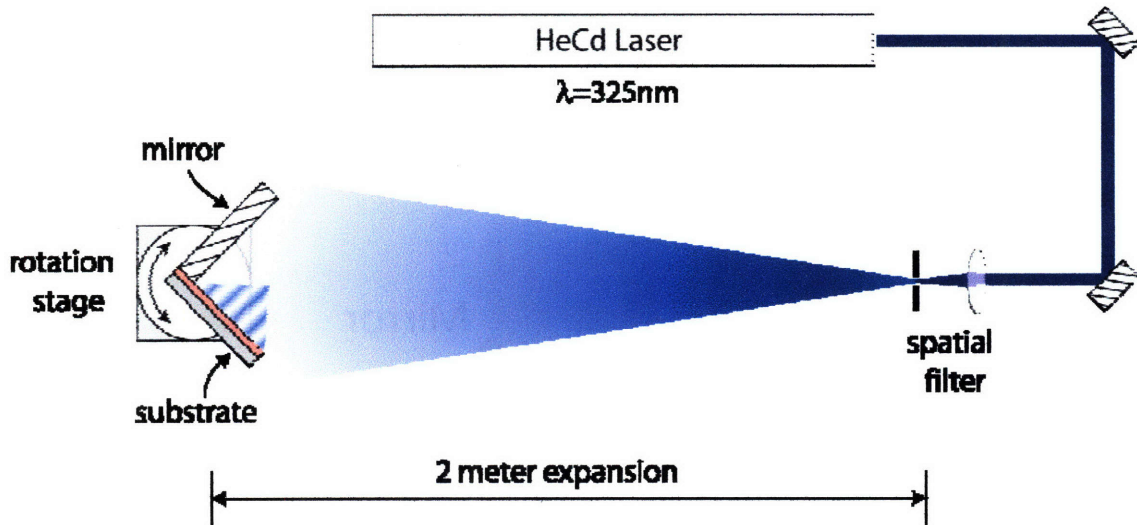
Figure 3.9: Illustration of the Lloyd's mirror interference lithography system. Adapted from [20].

Figure 3.9 illustrates the top view of a Lloyd's mirror IL system consisting of a 325 nm helium cadmium (HeCd) laser. Mirrors are used to direct the laser beam from the output of the laser to the spatial filter and to align the beam with the centre of the substrate/mirror assembly. The spatial filter is used to eliminate high frequency noise from the beam and results in a Gaussian beam whose intensity distribution is

$$I(r) = I_0 e^{\left(\frac{-2r^2}{\omega_0^2}\right)} \tag{3.34}$$

where I_0 is the intensity at the centre of the beam, r is the radial position from the centre of the beam and ω_0 is the beam waist [19]. A plot of the normalized Gaussian beam intensity is shown Fig. 3.10. The fact that the beam is Gaussian means that the incident irradiation varies over the sample. However, the beam travels approximately 2 meters from the spatial filter to the sample which causes it to expand so that at the sample the variation in intensity is not significant for the relatively small samples of interest. Also, the large distance between the spatial filter and the sample allows the radius of the beam diameter to increase which results in the beam more closely

approximating a plane wave at the substrate. However, a side effect of increasing the distance is that the intensity of the beam at the sample decreases and so a longer exposure time is required to obtain the same dose in the PR. Therefore, the choice of distance between the spatial filter and the sample is a tradeoff between pattern fidelity and exposure area versus exposure time.
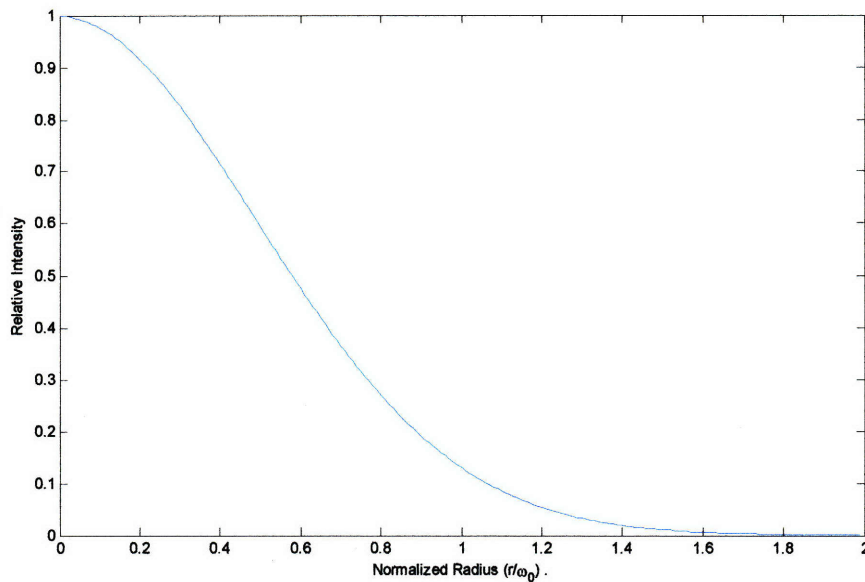
Figure 3.10: Normalized Gaussian beam intensity output from the spatial filter in the Lloyd's mirror IL system where r is the radial position from the centre of the beam and ω_0 is the beam waist.

The optical configuration at the substrate/mirror stage in the Lloyd's mirror IL system has a major impact on the performance of the system. An aluminium mirror is used because it exhibits relatively constant reflectivity over the range of angles of interest and exhibits very high reflectivity at 325 nm. Also, the mirror is relatively large, 5 inches by 5 inches, in order to avoid edge effects as a result of scattering from the mirror. The axis of rotation of the stage is set to the point at which the substrate and mirror intersect so that by simply adjusting the angle of the stage the spatial period of the grating can be changed. The optical axis of the incident beam is also set to

the point where the substrate and mirror intersect so that if the period of the grating is changed no optical alignment is necessary.

It is possible to form arbitrary patterns using the Lloyd's mirror IL system by performing multiple exposures at different angles and durations. As noted previously, to form a grid two orthogonal exposures must be performed for the same duration. It must be stated that the smallest feature which can be patterned using the Lloyd's mirror set-up described above is half the wavelength of the incident light. An in-depth analysis of the Lloyd's mirror IL system is given in [20].

3.4   Anti-Reflection Coating

ARC's are used in numerous applications to reduce the reflection of the incident light. In the case of Lloyd's mirror IL exposures, a standing wave normal to the surface of the substrate occurs due to the interference between the vertical component of the incident light and the reflection of light from the layers underneath the resist. The vertical standing wave causes unwanted patterning of the walls of the PR which reduces the repeatability of the process and causes problems in the pattern transfer stage. However, it is possible to reduce the magnitude of the vertical standing wave by adding a layer of ARC between the PR and the substrate. The ARC layer uses a combination of both absorption and interference to reduce the vertical standing wave. The two important characteristics of the ARC layer are its thickness and index of refraction.
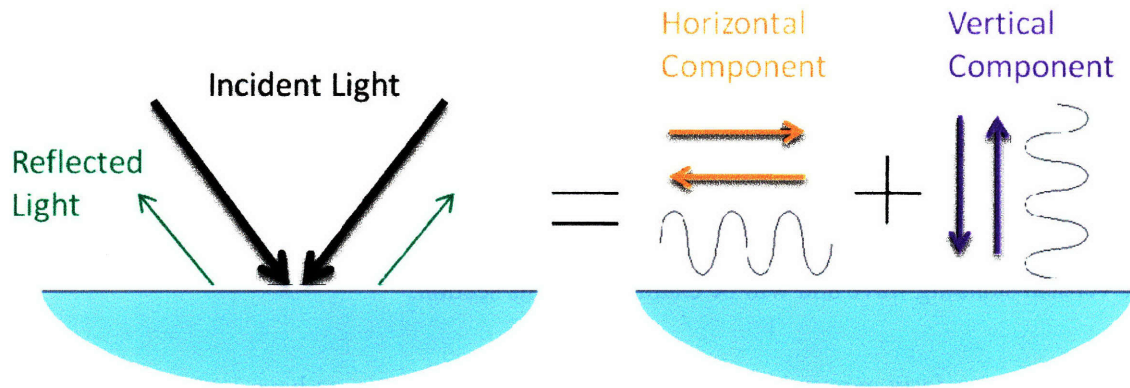
Figure 3.11: The incident and reflected light decomposed into a horizontal and vertical component.

Figure 3.11 shows how the incident and reflected light can be decomposed into a horizontal and vertical component. The period of the horizontal standing wave determines the period of the grating. While the period of the vertical standing wave, p_v, determines the period of the unwanted vertical pattern in the side walls of the PR and is given by

$$p_v = \frac{\lambda}{2ncos(\theta)} \tag{3.35}$$

where λ is the wavelength of the light, θ and the angle of incidence and n is the refractive index of the PR [16].

3.4.1 Index of Refraction

The magnitude of the vertical standing wave is highly dependent on the index of refraction of the ARC, N_{ARC}. The index of refraction is complex and can be represented in cartesian coordinates as

$$N_{ARC} = n_{ARC} + jk_{ARC} \qquad (3.36)$$

where n_{ARC} is the real part of the index of refraction which accounts for refraction and k_{ARC} is the imaginary part of index of refraction and accounts for absorption. The relation between N_{ARC} and the refractive index of the PR, N_{PR}, and the absorption of the ARC have a significant impact on the vertical standing wave and will be examined in this section.

In order for a uniform exposure to occur throughout the PR N_{PR} must have very low absorption and so N_{PR} is mostly real. In the case of index matching N_{ARC} and N_{PR}, it is valid to assume that they are both real and reduce to n_{ARC} and n_{PR} respectively. The equation for reflection, R, for two semi-infinite layers with real refraction indices is

$$R = \left[\frac{n_{ARC} - n_{PR}}{n_{ARC} + n_{PR}} \right]^2 \qquad (3.37)$$

which will evaluate to zero when the ARC and PR are perfectly matched [19]. However, in reality the layers are of finite thickness and there is a substrate below the ARC. Therefore, if n_{ARC} and n_{PR} are equal then they appear as one layer and any reflected light from the substrate will also reflect back into the PR. Therefore, index matching of the PR and ARC is highly undesirable.

The absorption of the ARC is very significant and if it is high then it will reduce the magnitude of the light traveling through the ARC. However, the light must first get coupled into the ARC. Considering again the case of semi-infinite layers of ARC and PR but this time taking into account the absorption term, the reflection, R, is given by

$$R = \frac{(n_{ARC} - n_{PR})^2}{(n_{ARC} + n_{PR})^2 + (k_{ARC} + k_{PR})^2} + \frac{(k_{ARC} - k_{PR})^2}{(n_{ARC} + n_{PR})^2 + (k_{ARC} + k_{PR})^2} \qquad (3.38)$$

which has been separated to illustrate the effects of the real and imaginary components of the index of refraction [19]. Therefore, the total reflection is dependent on the mismatch between the real parts and also the imaginary parts of the refractive indices of the two materials. Thus, it is possible for an ARC to cause high reflection as a result of a large mismatch in the absorption of the ARC and PR. However, in reality a specific ARC is chosen not based on its index of refraction but rather on the processing steps which occur after lithography.

3.4.2   Thickness Calculation

It is quite straightforward to solve for the reflection in the case of two semi-infinite layers, equation (3.38). However, when fabricating devices there are usually multiple metal and dielectric layers of varying thickness in which case the calculation of reflection becomes quite complex [19]. A simulation based on a transmission line model was developed in [16]. It plots the reflection back into the PR as a function of the ARC thickness for a stack of thin film layers. Once the refractive indices of all the materials in the stack are known and the thickness of each layer in the stack except the ARC has been determined it is possible to calculate the optimum thickness of the ARC to minimize the reflection back into the PR. This is discussed further in Section 4.1.2.

3.5   Photoresists

As mentioned in Section 3.3.1, PR's are polymers in which the solubility changes as a result of the applied dose. The development of PR's has been pioneered by the semiconductor industry in order to decrease the feature size of integrated circuits but there are many other applications in which PR's are used [21]. In each application there are many factors which determine the suitability of a specific PR, including the properties of the PR itself. The most important photoresist properties include contrast, transparency, adhesion and dose. The contrast of a PR is a measure of the how closely the PR exposure matches a binary response. A high contrast PR is one which transitions between exposed and unexposed as a result of quite a small difference in exposure dose.

It is desirable for the PR to be transparent enough so that the lower portion of the resist experiences the same dose as the upper portion of the resist. However, some absorption must occur within the PR in order for exposure to take place. Therefore, a trade-off must be made between uniformity of the pattern throughout the resist and the absorption which is essential for exposure. The need for transparency has been one of the major areas of PR research in the semiconductor industry.

Adhesion is sometimes a problem with PR's because most of them do not adhere well to hydrophilic surfaces such as silicon dioxide, so an adhesion promoter such as hexamethyldisilizane (HMDS) must be used. By spinning HMDS on the surface, a monolayer forms which converts the surface from hydrophilic to hydrophobic, which most PR readily adheres to.

3.5.1 Dose

The dose is commonly calculated by multiplying the exposure time, t_E, by the intensity of the incident radiation, I_I, from the laser beam (3.39). However, in the case of the Lloyd's mirror IL system this method is only valid for a specific grating period and resist stack. Therefore, a more detailed calculation must be performed in order for it to be possible to calculate the dose required to form a grating of any period.

$$D_I = I_I t_E \tag{3.39}$$

The dose calculated by multiplying the exposure time by the intensity of the incident radiation is actually is not the dose that the PR experiences. It is the incident dose, D_I, and is usually much higher than the actual exposure dose in the PR, D_E. To calculate D_E the reflectivity of both the top and bottom surfaces of the resist and the angle of the incidence of D_I must be taken into account. The reflection off the top surface of the PR, R_T, determines the amount of incident light that gets coupled into the PR. D_E is directly proportional to $1 - R_T$ and so it is desirable to minimize the surface reflection in order to reduce the required exposure time. The reflection from the layers beneath the PR, R_B, is directly related to D_E by $1 + R_B$ and as discussed in Section 3.4 this reflection is undesirable and a layer of ARC is usually used to minimize its effect. The angle of incidence of the beam, θ, the same angle defined in Fig. 3.8, has an impact on R_T and R_B. Also, as the angle of incidence increases the cross-section of the substrate in the beam deceases so the density of incident light on the surface of the PR decreases and so D_E is directly proportional to $\cos(\theta)D_I$. By taking all the above observations into account it is possible to formulate an equation for D_E such that

$$D_E = (1 - R_T)(1 - R_B)D_I \cos(\theta) \tag{3.40}$$

Once the value of D_E has been calculated under a specific set of conditions it is possible to calculate the required exposure time for any period grating and substrate by

$$t_E = \frac{D_E}{I_I(1 - R_T)(1 - R_B)\cos(\theta)} \tag{3.41}$$

The effect of variations in resist thickness on D_E is non-linear and quite complex to analyze and it must be noted that (3.41) does not take it into account [16].

3.6   Reactive Ion Etching

RIE is a plasma-based dry etching subtractive pattern transfer technique used in the fabrication many devices such as transistors, displays and photonic crystals [10]. Numerous RIE reactor geometries have been developed [22]. Figure 3.12 illustrates the basic configuration of a parallel-plate RIE reactor in which a plasma forms between the two parallel-plate electrodes. Power from an RF generator is capacitively coupled to the cathode electrode which results in it becoming negatively DC biased relative to the anode electrode which is at ground. The substrate is placed on top of the cathode and so ion bombardment of the substrate occurs.
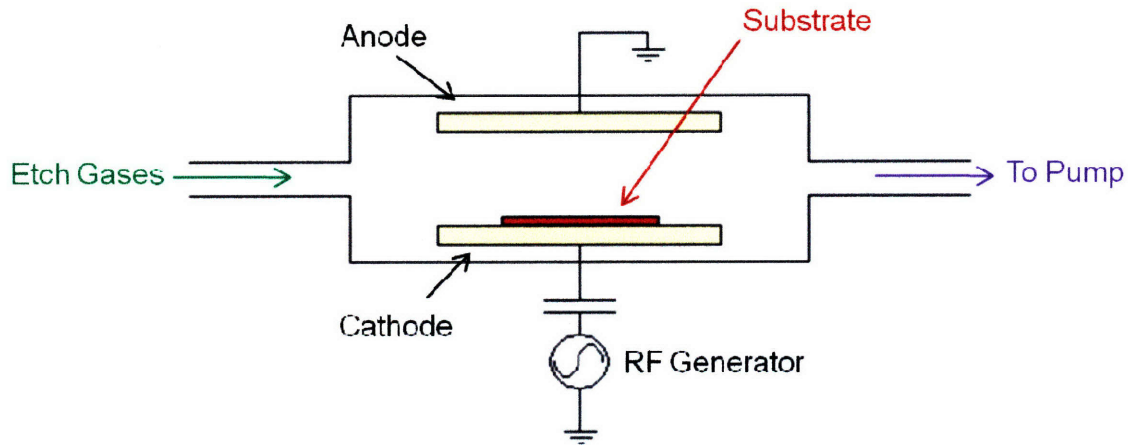
Figure 3.12: Parallel-plate RIE reactor.

As illustrated in Fig. 3.13, there are essentially six stages in the RIE process. The first and second stages of RIE are very similar to the first two stages of PECVD, discussed in Section 2.1, specifically the generation of reactants within the plasma and the transport of the reactants to the surface. However, once absorption of the reactants takes place, step 3, very different surface reaction takes place. In an RIE system the reaction, step 4, results in the desorption of part of the substrate, step 5, and this produces volatile species. Finally, the volatile species are removed, step 6, from the surface and subsequently from the chamber. Note that it is possible to enhance the reaction of the neutral reactants with the surface by use of ion bombardment.
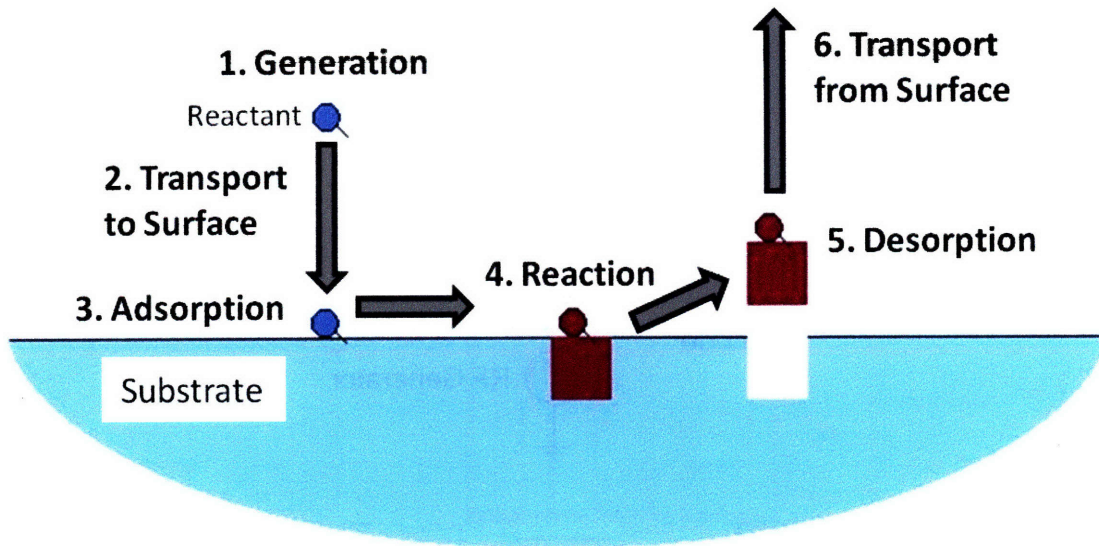
Figure 3.13: The six basic stages of the RIE process: 1. generation of reactants, 2. transport of reactants to the surface of the substrate, 3. absorption of reactants to the surface of the film, 4. reaction between reactant and the substrate, 5. removal of the product of the reaction and 6. transport of products away from the surface of the substrate.

The four major considerations in an RIE based etch are the etch rate, mask resistance, selectivity and directionality. The etch rate is a measure of the volume of the substrate removed per unit time. As mentioned above, in order for etching to take place adsorption, a reaction and desorption must occur. It is possible to change the etch rate by changing the gas concentrations by blocking any of these stages from occurring or the amount of ion bombardment. The mask resistance is a measure of the durability of the mask during etching of the substrate. The selectivity of an etch process is a comparison between the etch rates of the substrate and the mask. The selectivity is related to the mask resistance, both of which are highly dependent on the etch gases and the amount of ion bombardment. The directionality of an etch is a measure of the anisotropy of the etch, where an anisotropic etch is one in which etching takes place preferentially in one direction whereas an isotropic etch takes place equally in all directions. The directionality of an etch is crucial to maintaining accurate pattern transfer of features from the mask to the substrate. Figure

3.14 illustrates both an anisotropic and isotropic etch taking place in a substrate. It is possible to increase the directionality of an etch by sidewall coating or by increasing ion bombardment.

There are a number of variables in an RIE system which can be adjusted in order to tailor an etch to match specific requirements. These include the temperature of the substrate, chamber pressure, gas flow rates, gas concentrations, and the RF generator frequency and power. A lot of the considerations mentioned above are inter-related in terms of the variables that control them and so a trade-off must be made in order to achieve the desired pattern transfer.
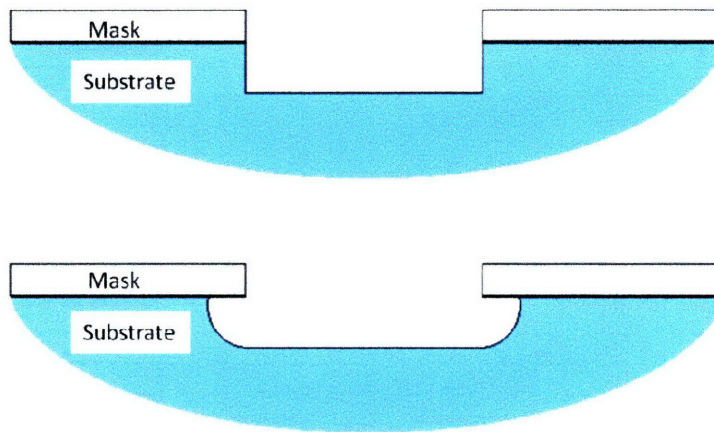
Figure 3.14: Anisotropic (top) and isotropic (bottom) etch.

Resonant Thermal Emitter Fabrication

The goal of this chapter is to describe the fabrication procedure of the resonant thermal emitter 2-dimensional silicon-on-sapphire (SOS) photonic crystal structure discussed in Chapter 2, Fig. 4.1. The specifications of this structure include a periodicity, *a*, of 1 μm, a hole radius, *r*, of $r = 0.2a = 200$ nm and hole depth, *d*, of $d = a/2 = 500$ nm. The subsequent sections give an in-depth description of the three main fabrication stages which use the technologies described in Chapter 3. The first fabrication stage is the deposition of the different layers of material in the stack and involves the use of CVD and spin coating. The second fabrication stage is the lithographic formation of the desired pattern of holes by Lloyd's mirror interference lithography. Finally RIE is used to complete the final fabrication stage which is the etching of the pattern of holes into the other layers in the stack.
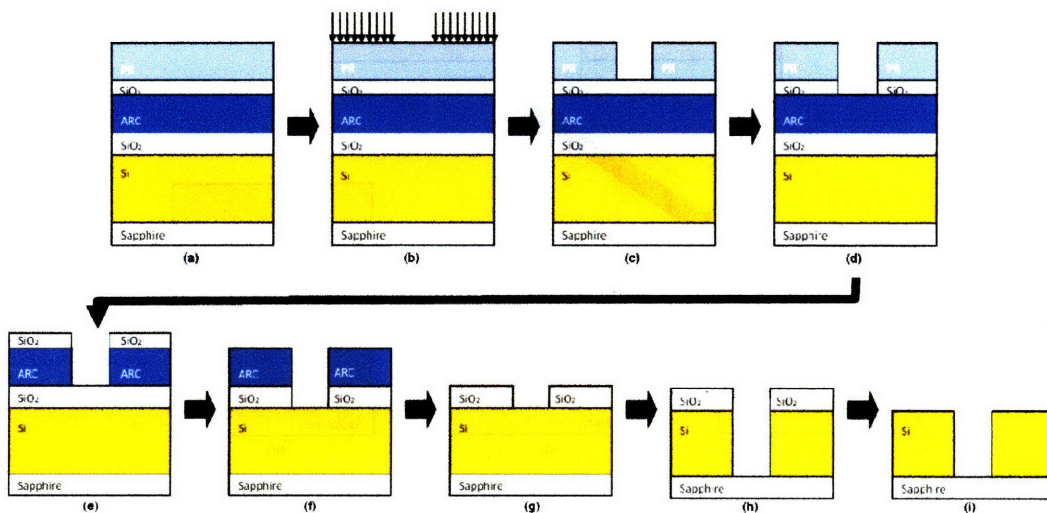
Figure 4.1: Fabrication procedure for the 2-dimensional silicon-on-sapphire photonic crystal structure.

4.1   Deposition

The first stage in the fabrication of the 2-dimensional SOS resonant thermal emitter is the deposition of the different layers of material in the stack as shown in Fig. 4.1 (a) and Fig. 4.2. As mentioned previously silicon is deposited on top of a sapphire substrate which is then patterned to form a photonic crystal. The 2-dimensional silicon structure forms a metamaterial with emission peaks, while the sapphire offers the unique property of being almost transparent up to 6 μm which is significant because it transmits nearly all the emitted photons. The silicon is deposited on sapphire by molecular beam epitaxy and forms a 600 nm thick layer of <100> intrinsic type silicon on a 530 μm thick sapphire substrate. The silicon on sapphire substrates are provided by Valley Design Corp, California, USA. It should be noted that the silicon-on-sapphire substrates are not cleaned in advance of deposition as it has been found that cleaning can damage the silicon which results in silicon etching problems.
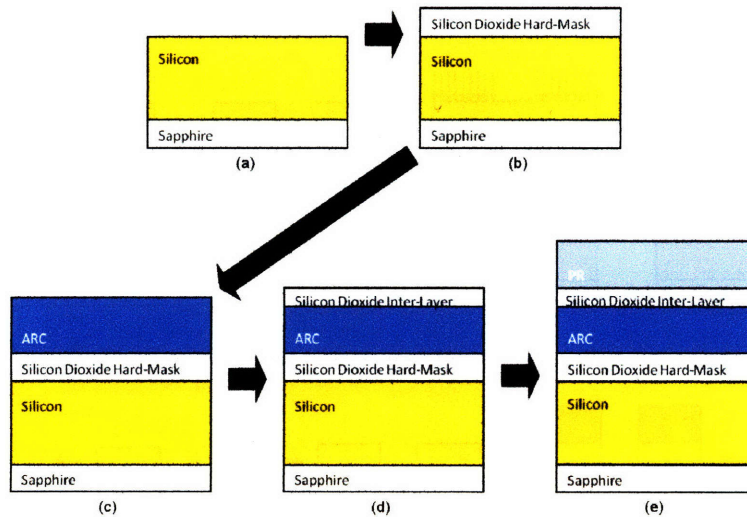
Figure 4.2: The deposition stages: (a) silicon on a sapphire substrate; (b) silicon dioxide hard-mask deposition on the silicon; (c) ARC spin coated on the silicon dioxide hard-mask; (d) silicon dioxide inter-layer deposited on the ARC; (e) PR spin coated on the silicon dioxide inter-layer.

The purpose of the other four layers in the stack is to enable the patterning of holes in silicon. The first layer is a relatively thick layer of silicon dioxide, the hard-mask, which is directly deposited onto the silicon substrate using PECVD, Fig. 4.2 (b). The second layer is ARC which is spin coated on top of the silicon dioxide hard-mask layer, Fig. 4.2 (c). The third layer is a relatively thin layer of silicon dioxide deposited, again using PECVD, as an inter-layer between the ARC and PR, Fig. 4.2 (d). Finally, a layer of PR is spin coated on top of the silicon dioxide inter-layer, Fig. 4.2 (e). The thicknesses of each layer is primarily chosen so that it can act as a mask for etching the layer beneath it. However, as discussed in Section 4.1.2 there are other factors which affect the choice thickness in the case of ARC. The deposition of each of these layers will be discussed in the next four subsections.

4.1.1   PECVD Silicon Dioxide Hard-Mask

In order to etch deep holes in silicon it is necessary to have a mask which etches at a very slow rate relative to silicon. This mask is referred to as the hard-mask and it has been found that in certain chemistries the selectivity of silicon to silicon dioxide is quite high. Therefore, a relatively thick layer of silicon dioxide was chosen to act as the hard-mask in the fabrication of the SOS resonant thermal emitter.

The silicon dioxide hard-mask was deposited onto the SOS substrate, Fig. 4.2 (b), using the Surface Technology Systems (STS) PECVD system in the Technology Research Laboratory (TRL) at MIT. The STS PECVD is a common tool used in industry to deposit a range of highly uniform organic and inorganic films at low temperature and pressure. The TRL STS PECVD can be used to deposit films of silicon dioxide, silicon nitride, silicon carbide, amorphous silicon and phos-

phorous-doped amorphous silicon. The system consists of one chamber in which deposition takes place, a load lock mechanism for loading the samples and a central terminal which can be used to program specific recipes. The samples can be wafers up to 6" in diameter or wafer pieces.

There are many variables on the STS PECVD system which can be adjusted to control the film type and deposition rate. The type of film which is deposited is primarily determined by the composition of gases in the chamber. The gases available on the STS-CVD include nitrogen, oxygen, silane, methane, nitrous oxide, argon, ammonia and tetrafluoromethane. It is possible to control the pressure within the chamber as well as the temperature of the gases both as they enter the chamber and at the substrate. Also, the RF generator power and frequency can be adjusted along with the duration of time that power is applied.

Thin silicon dioxide films are used in the fabrication of many devices, including integrated circuits, which has resulted in numerous publications analysing the effects of each of the PECVD variables on the deposition of silicon dioxide films [19], [24], [25]. Although the publications used different configurations the results are worth noting. It has been demonstrated that the RF power plays an important role in the structure of the film at an atomic level and that as expected the quality of the film is directly proportional to the RF power [19]. However, it has been shown that temperature has a bigger effect on the film quality and although the deposition rate stays constant with temperature, the refractive index, a function of the film quality, approaches its expected value at higher temperatures [19], [24]. It has also been shown that the deposition rate varies within the chamber and that the percentage of the gases relative to each other has a major effect on the growth rate [25].

In order to deposit the silicon dioxide hard-mask in the TRL PECVD a mixture of 10 sccm of silane, 392 sccm of nitrogen and 1420 sccm of nitrous oxide is used. The pressure is set to 900 mTorr while the temperature is set to 250 °C at the showerhead and 300 °C at the substrate. An RF frequency of 13.56 MHz and a power of 30 W is used to generate the plasma. All the parameters are listed in Table A.1 in Appendix A.

The deposition rate of the PECVD system changes depending on the previous depositions which took place in the chamber. Therefore, a characterization run must be performed in order to determine the deposition rate before performing deposition on the real sample. The calibration run involves preparing the chamber by performing a 3 minute deposition with no sample in the chamber so as to coat the chamber with silicon dioxide thus reducing contaminants. After preparing the chamber, depositions are performed on dummy silicon wafer pieces at three specific times, namely one minute, two minutes and three minutes. The film thickness at each of these times is then measured using a NanoSpec tabletop film analysis system in TRL. The deposition rate is calculated by graphing the deposition thicknesses versus time and interpolating along the graph to find the time required to deposit 100 nm. The reason this calibration technique can be used is that the thickness of the film varies linearly with time which is verified in Fig. 4.3. Figure 4.3 is a plot of the deposited silicon dioxide film thickness for eleven PECVD deposition times separated by ten seconds. Each of the silicon dioxide thickness measurements were performed on silicon substrates and the measurements were taken using the TRL NanoSpec. In the case of Fig. 4.3, the deposition rate of silicon dioxide is around 46 nm/min. Once the deposition rate is known the film thickness is controlled by the duration of the plasma. Therefore, in order to deposit a layer of silicon dioxide that is 100 nm thick, a deposition time of around 2 min: 10 s is required.

Appendix A lists all the process parameters which were set on the TRL PECVD to achieve this deposition rate.
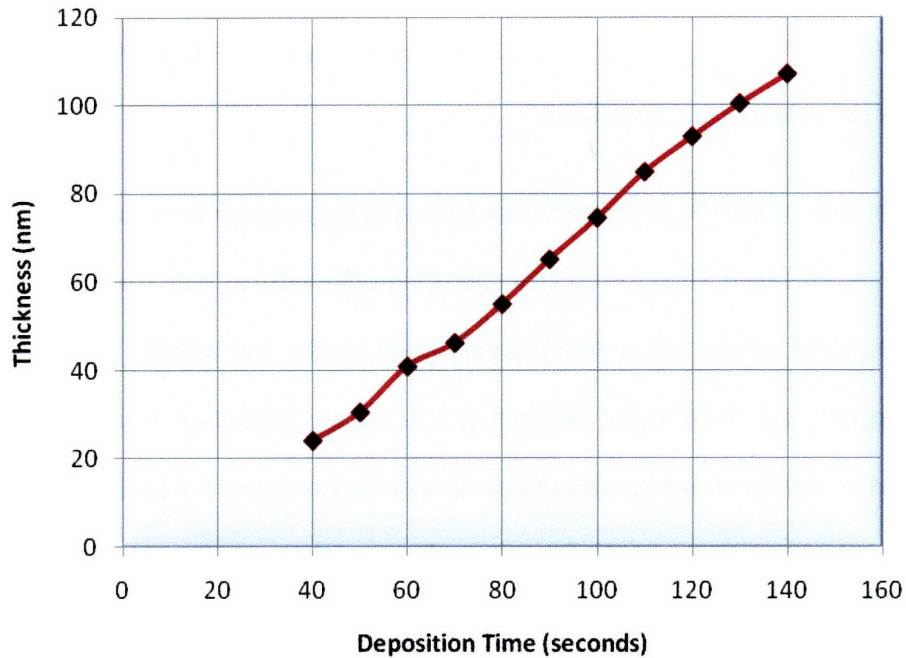
Figure 4.3: Silicon dioxide thickness versus deposition time for PECVD.

4.1.2   Spin Coating Anti-Reflection Coating

As stated in Section 3.4, reflection from the layers beneath the PR can cause undesired exposure of the PR. However, it is possible to reduce the amount of reflection from the layers beneath the PR by adding a layer of ARC beneath the PR. The ARC layer is usually a polymer which is spin coated onto the surface of the substrate. In the spin coating of ARC the first processing step involves applying an excess amount of the liquid ARC polymer onto the surface of the substrate to be coated. Then the substrate is accelerated to the desired speed and allowed to rotate at a con-

stant speed for a specified amount of time. The theory behind spin coating was examined in Section 3.2.
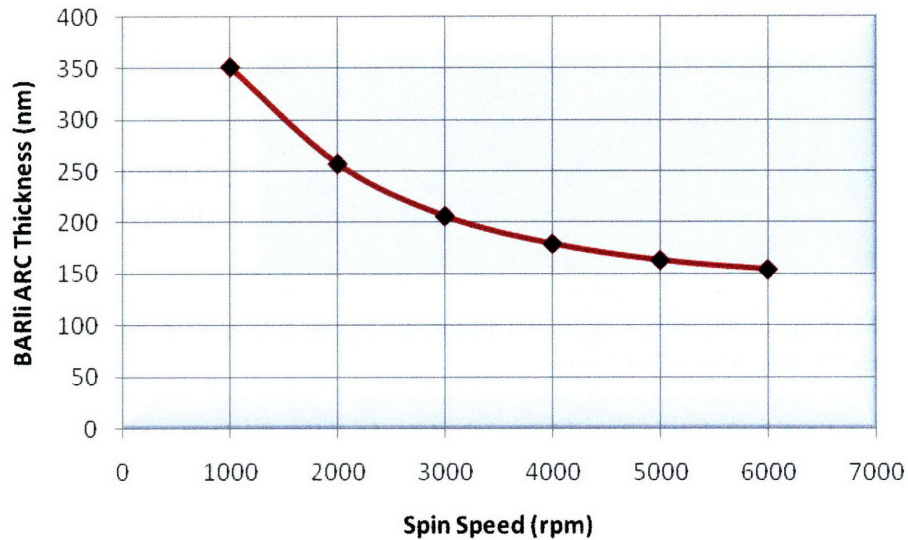
Figure 4.4: Spin curve for BARLi ARC showing the relationship between ARC thickness and spin speed.

The ARC used in the fabrication of the 2-dimensional SOS resonant thermal emitter is a cyclohexanone-based polymer called AZ(R) BARLi which is manufactured by AZ Electronic Materials USA Corp, New Jersey, USA. In order to determine the required spin speed for a specific ARC thickness a spin curve calibration was performed, Fig. 4.4. This involved spinning ARC on a substrate, with a silicon dioxide surface, at various spin speeds and then using a scanning electron microscope (SEM) to view the cross-section of the substrate from which the ARC thickness is measured. A typical SEM cross-section is shown in Fig. 4.5. All the SEM images in this thesis were obtained using the NSL Zeiss/Leo Gemini 982 SEM.
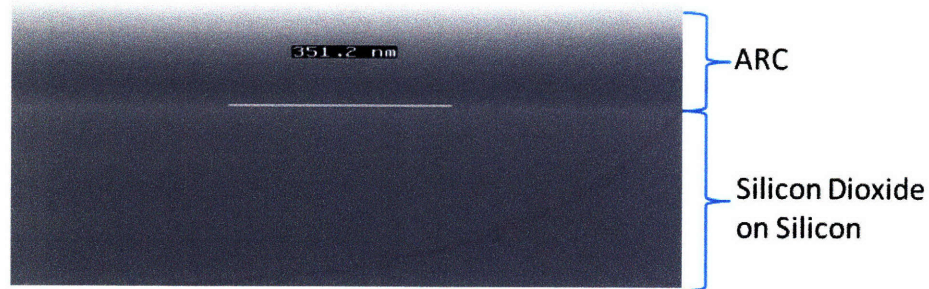
Figure 4.5: SEM image of the cross-section of a silicon dioxide on silicon wafer spun with ARC at 1000 rpm showing an ARC thickness of 351.2 nm.

As mentioned in Section 3.4, it is possible to calculate the ARC thickness which will result in the minimum back reflection into the PR. This calculation is dependent on the wavelength and angle of the incident light, as well as the thickness and refractive indices of each layer in the stack. In the case of the SOS resonant thermal emitter fabrication the angle of incidence is 0.163 rad. The thicknesses of the layers are as follows, 190 nm PS4 PR, 20 nm silicon dioxide inter-layer, 100 nm silicon dioxide hard-mask, 600 nm silicon on a 530 μm sapphire substrate. The refractive indices for the materials in the stack at 325 nm are given in Table A.2 in Appendix A. Based on these parameters a software simulation similar to the one developed in [16] was used to plot the reflectivity as a function of ARC thickness at the interface of the PS4 PR and the silicon dioxide inter-layer. The result of this simulation is shown in Fig. 4.6 which shows that the absolute minimum reflection, 0.2%, occurs at an ARC thickness of 153 nm. Although the primary purpose of the ARC layer is to reduce back reflection into the PR, it also serves as a mask for the silicon dioxide hard-mask etch. Therefore, the thickness of the ARC layer was chosen to be 257 nm

which is the thickness that corresponds to the third minimum in Fig. 4.6 and is also sufficiently

thick to act as a mask for etching the silicon dioxide hard-mask. In order to calibrate some of the

fabrication processes silicon wafers were used instead of SOS substrates. The reflectivity simula-

tion was performed for the case of the monitor wafers and it was found that the substrate actually

caused relatively no change in the reflectivity at the boundary between the PR and silicon dio-

xide inter-layer and so the same ARC thickness was used for the monitor wafers.
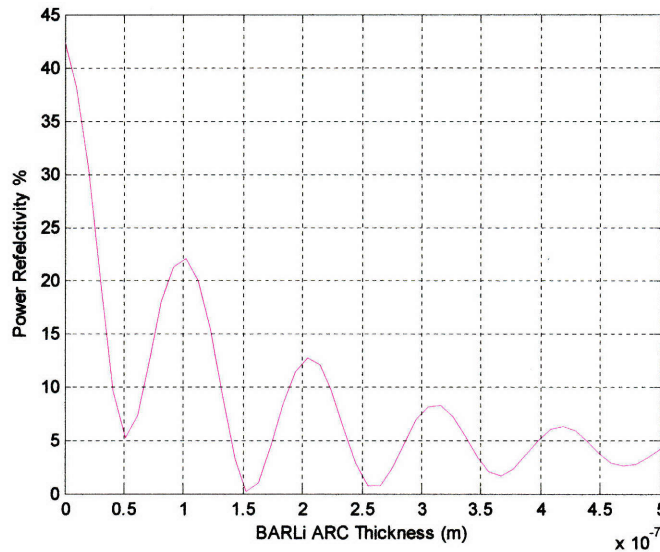
Figure 4.6: Reflectivity plotted as a function of BARLi ARC thickness at the interface of the PS4 PR and the silicon dioxide inter-layer for a 325 nm TE polarized wave incident at an angle of 0.163 rad on a stack consisting of 190 nm PS4 PR, 20 nm silicon dioxide inter-layer, BARLi ARC, 100 nm silicon dioxide hard-mask, 600 nm silicon on a 530 μm sapphire substrate.

The spin speed required to obtain an ARC thickness of 257 nm is calculated from the spin curve

in Fig. 4.10 and is found to be 2,000 rpm. After spin coating the BARLi ARC onto the sample at

2,000 rpm for 60 second using the TRL PMMA spinner the sample is then baked at 175 ˚C for

ninety seconds. Table A.3 in Appendix A lists the parameters for BARLi ARC spin coating and

softbake.

4.1.3   PECVD Silicon Dioxide Inter-Layer

The PS4 PR and BARLi ARC both etch in the same chemistry and so PR is not a sufficient mask for etching ARC. However, silicon dioxide does not etch in the same chemistry as that used to etch ARC. Therefore, to facilitate the accurate pattern transfer from the PR into the other layers in the stack a thin layer of silicon dioxide is added between the ARC and PR, an inter-layer. This results in a tri-layer resist stack which is the term used to collectively describe the ARC, silicon dioxide inter-layer and PR. The thickness of the silicon dioxide in the tri-layer resist stack is selected so that it can act as a mask for the ARC etch. In the case of the resonant thermal emitter a 20 nm layer of silicon dioxide is deposited using PECVD in TRL. The deposition time required to deposit 20 nm of silicon dioxide inter-layer was found to be 0 min: 25 s. The deposition parameters are the same as in the case of depositing the silicon dioxide hard mask, Section 4.1.1, except a lower temperature, 150 °C, is chosen so as not to damage the ARC. The parameters are listed in Table A.1 in Appendix A.

4.1.4   Spin Coating Photoresist

The PR is the final layer to be deposited in the stack. It is spin coated on top of the silicon dioxide inter-layer and the desired pattern is transferred into the photoresist using lithography. The process of spin coating PR is very similar to ARC spin coating which was discussed in Section 4.1.2 and the theory behind spin coating was investigated in Section 3.2. The PR used in the fabrication of the 2-dimensional SOS resonant thermal emitter is a negative resist polymer known as THMR-iN PS4 which is manufactured by OHKA America, Oregon, USA. A spin curve calibration was performed to determine the required spin speed for a specific PR thickness, Fig. 4.7.

The spin curve was obtained by spinning PR on a substrate, with a silicon dioxide surface, at various spin speeds and then measuring the thickness for each spin speed using an SEM, Fig. 4.8.
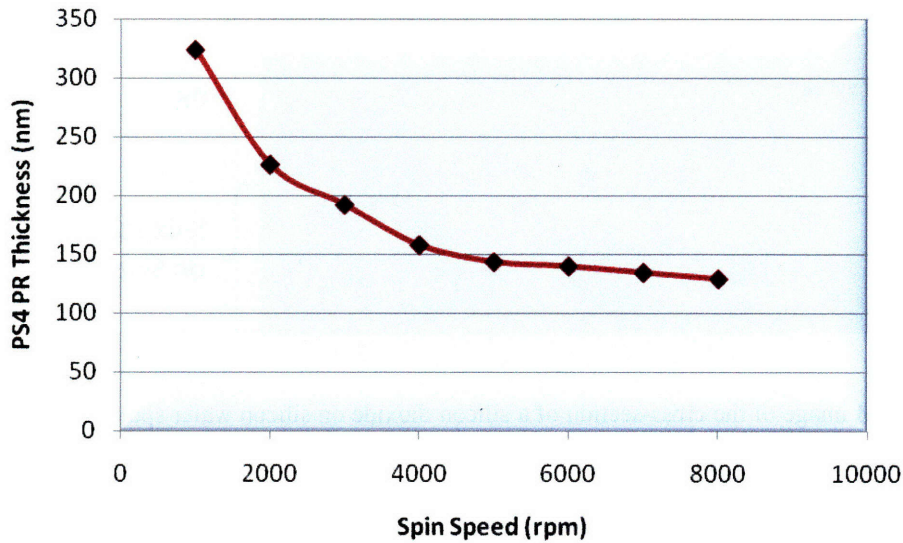
Figure 4.7: Spin curve for PS4 PR showing the relationship between PS4 PR thickness and spin speed.

The choice of PR thickness is a trade-off between contrast and pattern transfer fidelity. If the PR is too thick then the top of the PR will experience a different dose than the bottom of the resist and so contrast will be reduced. However, if the PR is too thin then it will not be able to act as a mask for the silicon dioxide inter-layer etch. A PR thickness of 190 nm was chosen for the fabrication of the SOS resonant thermal emitter which, from the spin curve in Fig. 4.7, requires a spin speed of 3000 rpm. The PR is spin coated onto the silicon dioxide interlayer at 3000 rpm for 60 seconds using the NSL spinner and then softbaked at 90 °C for 90 seconds. It is essential to perform the softbake step as it removes any residual solvent from the PR layer which would alter the quality of the film.
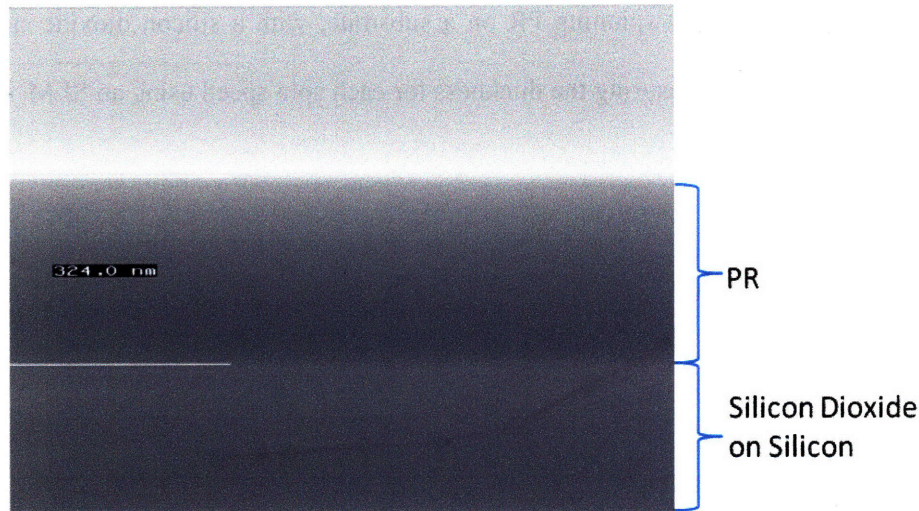
Figure 4.8: SEM image of the cross-section of a silicon dioxide on silicon wafer spun with PR at 1000 rpm showing a PR thickness of 324 nm.

It has been found that there are adhesion problems with spin coating PS4 PR directly onto silicon dioxide and so an adhesion promoter is used to prevent this problem. In the fabrication of the resonant thermal emitter hexamethyldisilazane (HMDS) is spin coated at 3000 rpm for 60 seconds onto the silicon dioxide inter-layer. The HMDS forms a monolayer on the surface of the silicon dioxide which converts the surface from hydrophilic to hydrophobic, which the PR readily adheres to. When HMDS is spin coated it releases ammonia in the process, this can contaminate the PS4 PR. Thus, after spin coating HMDS on the silicon dioxide inter-layer, a period of dreater-than 15 minutes must be waited before spinning the PR.

4.2 Lithography

The next stage in the fabrication procedure involves forming the desired pattern of holes by exposing the PS4 PR using the Lloyd's mirror interference lithography (IL) system in NSL, Fig. 4.1

(b). Figure 4.9 illustrates the lithography stage of the fabrication process including the exposure of the PR and the stack which results from exposure and development of the PR. The desired pattern for the specific SOS resonant thermal emitter design investigated in this thesis is a 1 μm period grid pattern of 0.4 μm diameter round holes. The theory behind IL and the Lloyd's mirror IL system were discussed Section 3.3.
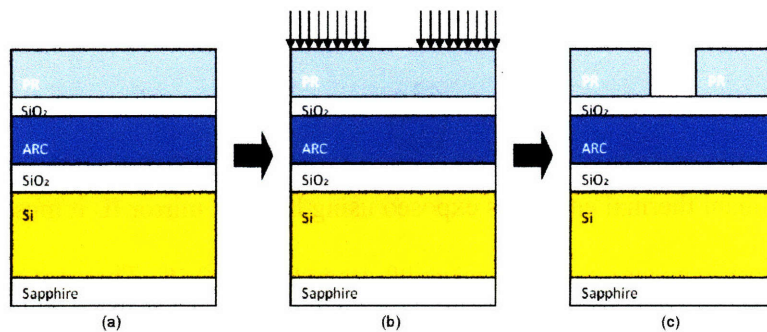
Figure 4.9: The lithography stages: (a) stack after the deposition stage; (b) expose PR using lithography; (c) stack after PR exposure and development.

4.2.1 Lloyd's Mirror Interference Lithography

Lloyd's mirror IL is an ideal lithography technique for exposing the SOS resonant thermal emitter since it is able to accurately expose relatively large areas with a periodic pattern in a short span of time. The specific configuration of the Lloyd's mirror IL system in NSL which is used in the fabrication of the resonant thermal emitter is shown in Fig. 3.9. This system uses a 325 nm wavelength laser as the source, a IK3501R-G HeCd Laser manufactured by Kimmon Electric US, Colorado.

The angle of the substrate holder relative to the incident beam, θ, is given by equation (4.1) where p is the desired periodicity of the structure and λ is the wavelength of the incident light. In

the case of the resonant thermal emitter the periodicity of the 2-dimensional photonic crystal is 1

μm and the wavelength of the beam is 325 nm so the desired angle of incidence is 0.163 rad. The

NSL Lloyd's mirror IL system substrate holder uses a vernier scale to set the desired angle but

due to the fact that the vernier scale is not perfectly aligned with the incident beam there is usu-

ally an offset. Therefore, in the case of the SOS resonant thermal emitter fabrication the vernier

scale was set to 0.127 rad in order to achieve the required 1 μm periodic structure.

$$\theta = sin^{-1}\left(\frac{\lambda}{2p}\right) \qquad (4.1)$$

After the SOS resonant thermal emitter is exposed using Lloyd's mirror IL it must be baked. This

is known as the post-exposure bake and takes 90 seconds at 110 °C. The post-exposure bake is

essential for PS4 as it causes chemical reactions to occur within the PR, without it the entire PR

including the exposed regions would be removed in the developer. The development of PS4 is

performed for 60 seconds in CD-26 manufactured by Rohm and Haas, Pennsylvania, USA. After

development the sample must be rinsed in deionized water to remove any remaining developer

and then dried with gaseous nitrogen. Table A.3 in Appendix A lists the parameters for PS4 PR

spin coating, softbake, post-exposure and development.

When forming holes with negative PR, the exposure dose is inversely proportional to the diame-

ter of the holes. As the laser power of the NSL Lloyd's mirror IL system varies on a daily basis,

the exposure time must be adjusted to obtain the required exposure dose. A characterization of the

PS4 PR was performed to determine the required dose to obtain 400 nm holes. Figure 4.10 shows

nine SEM images of the top of developed monitor wafers after exposure to doses from 5 mW-s to

45 mW-s with the Lloyd's mirror IL system. A graph of hole radius versus exposure dose from

the laser is given in Fig. 4.11, from which it is possible to determine that a dose of 17.8 mW-s is required to obtain the desired 400 nm diameter holes.
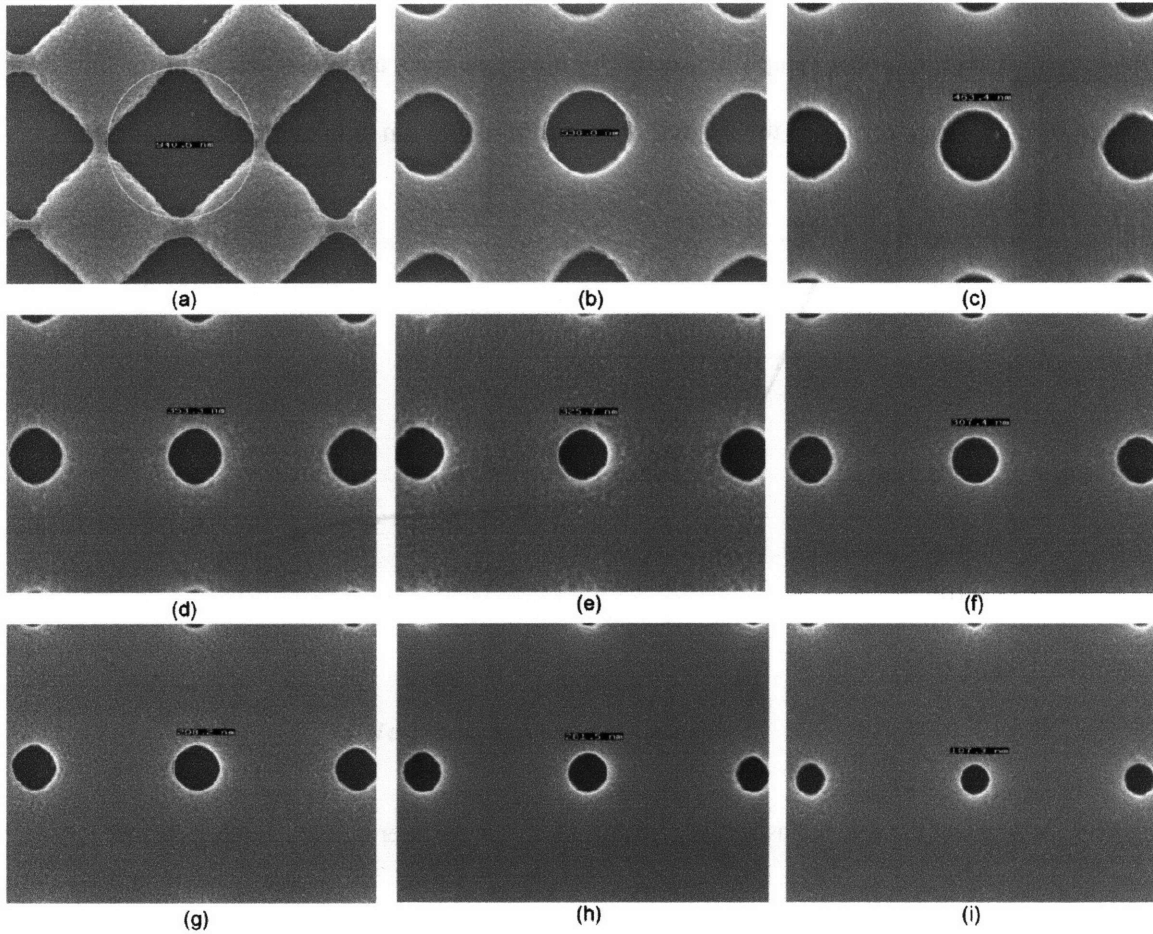
Figure 4.10: Top view SEM images of the developed monitor wafers after exposure doses of (a) 5 mW-s, (b) 10 mW-s, (c) 15 mW-s, (d) 20 mW-s, (e) 25 mW-s, (f) 30 mW-s, (g) 35 mW-s, (h) 40 mW-s and (i) 45 mW-s with the Lloyd's mirror IL system. The holes have a periodicity of 1 μm.

The values of exposure dose in Fig. 4.10 correspond to the dose incident from the laser beam at the substrate holder. It is possible to determine the dose experience by the PR as discussed in Section 3.3.1. As the SOS resonant thermal emitter fabricated in this research had a constant periodicity of 1 μm and the thickness of the layers in the stack is constant, it is possible to calculate the required dose directly from Fig. 4.11. In general the intensity of the incident light measured at

the substrate holder was around 130 μW, so to form 400 nm holes an exposure time of around 2 min: 47 s was needed. The NSL Lloyd's mirror IL system can only expose lines in PR so two perpendicular exposures must be performed to obtain a grid pattern. Therefore, after an initial exposure of 2 min: 47 s the sample is rotated by ninety degrees and exposed again for the same amount of time which results in the desired grid pattern of 400 nm diameter holes.
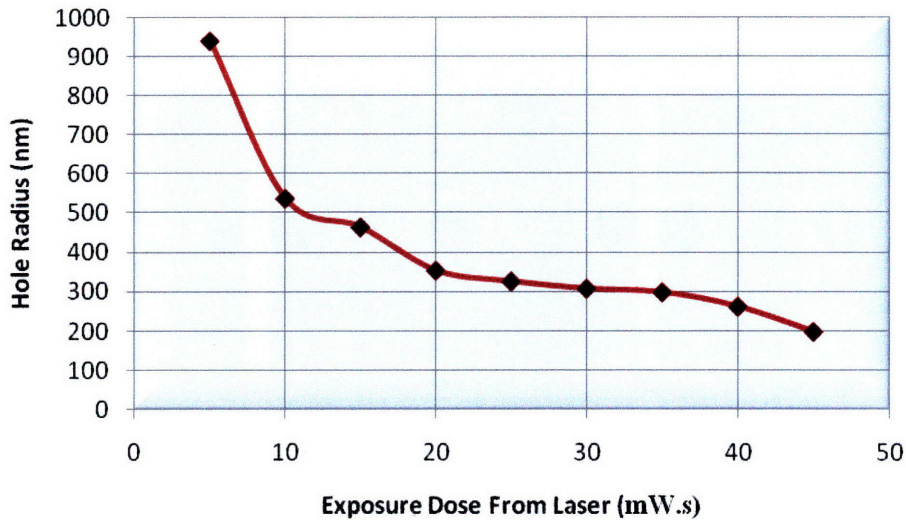
Figure 4.11: Graph of the hole radius versus exposure dose from the laser measured at the substrate holder.

4.3   Etching

The SOS resonant thermal emitter design under investigation requires 600nm deep holes in silicon. Thus, the final stage in the fabrication of the SOS resonant thermal emitter involves transferring the pattern of holes formed in the lithography stage into silicon, Fig. 4.1 (d) – (i). Figure 4.12 illustrates the etching stage of the fabrication process including the silicon dioxide inter-layer etch after the lithography stage, the ARC etch, the silicon dioxide hard-mask etch, the silicon etch and

finally the silicon dioxide hard-mask removal. All the etches are performed using RIE and in order to characterize the etch of each layer monitor samples are used. The monitor samples consist of the exact same stack as used for the resonant thermal emitter but a silicon wafer is used as the substrate instead of SOS. The process by which RIE takes place was discussed in Section 3.6.
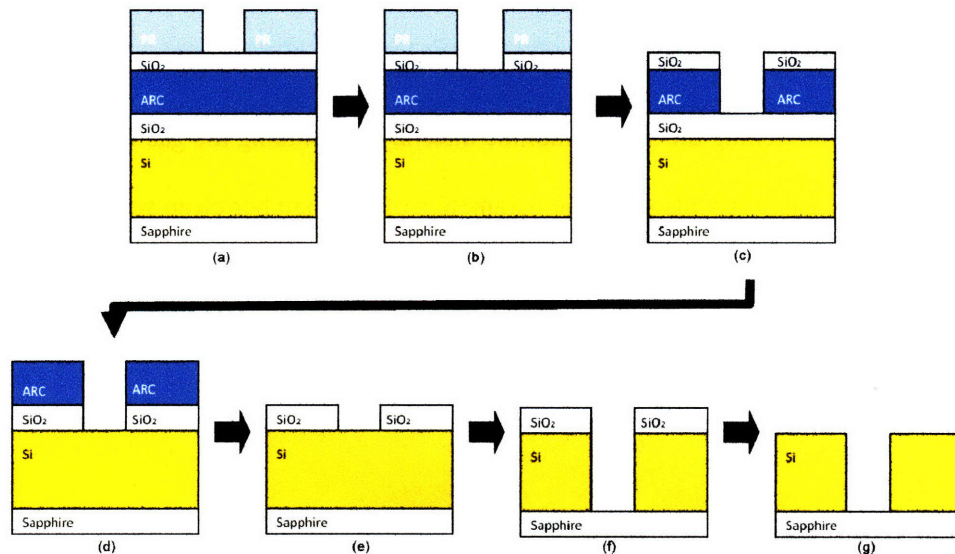
Figure 4.12: The etching stages: (a) stack after the lithography stage, (b) silicon dioxide inter-layer etch, (c) ARC etch, (d) silicon dioxide hard-mask etch, (e) ARC removal, (f) silicon etch, (g) silicon dioxide hard-mask removal.

4.3.1   RIE Silicon Dioxide Inter-Layer

The silicon dioxide inter-layer is etched using tetrafluoromethane (CF_4) gas in the PlasmaTherm 790 Series RIE System in NSL, Fig. 4.12 (b). Ideally the etch should stop after it has etched through the inter-layer. However, CF_4 also etches BARLi ARC and so the etch must be characterized in order to prevent excessively over-etching into the ARC. Figure 4.13 shows an SEM image of the cross-section of a monitor sample after a 30 s CF_4 etch in which the inter-layer has been etched through and some over-etching has occurred. It is prudent to slightly over-etch into the

ARC because variations occur in the etch rate due to the chamber conditions. However, excessively over-etching is not desirable either as it causes isotropic etching of the silicon dioxide inter-layer. The over-etching into ARC which occurs when a 2 min: 30 s CF_4 etch is performed is shown in Fig. 4.14. Therefore, an etch time of 30 s was chosen to etch through the 20 nm silicon dioxide inter-layer of the SOS resonant thermal emitter and the characterizations in the rest of this chapter occur after performing a 30 s silicon dioxide inter-layer RIE. Table A.4 in Appendix A lists the parameters for etching the silicon dioxide inter-layer including the gas flow rate, pressure and voltage setpoint. Table A.4 also lists the parameters of the chamber clean which is performed, with no sample in the chamber, before every silicon dioxide inter-layer etch. The chamber clean removes the oxides and organic contaminants from the chamber.
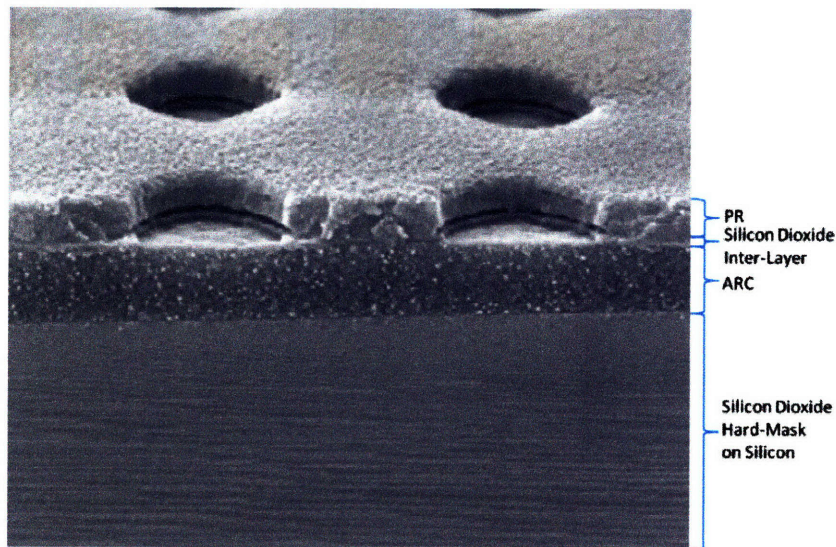
Figure 4.13: SEM image of the cross-section of a monitor sample after a 30 s RIE of the silicon dioxide inter-layer in CF_4. The holes have a periodicity of 1 μm.
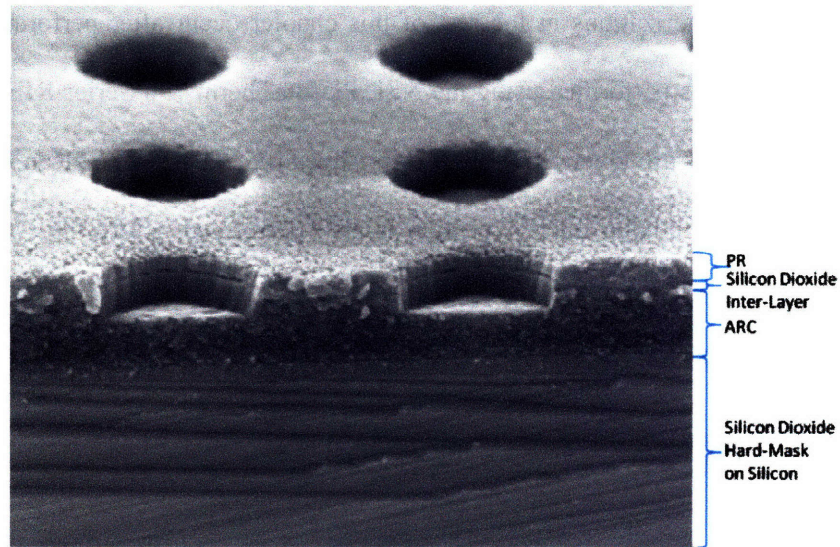
Figure 4.14: SEM image of the cross-section of a monitor sample after a 2 min: 30 s RIE of the silicon dioxide inter-layer in CF_4. The holes have a periodicity of 1 μm.

4.3.2   RIE Anti-Reflection Coating

After the silicon dioxide inter-layer has been etched the pattern of holes is transferred into the ARC layer using a mixture of helium (He) and oxygen (O_2) gases, Fig. 4.12 (c). These gases react with both the PR and ARC layers but not the silicon dioxide inter-layer. Thus, the silicon dioxide inter-layer acts as the mask for the etch of the ARC layer and the PR is etched away in the process. The ARC etch must be characterized to determine the etch time required to fully etch through 250 nm of ARC while preventing isotropic etching from occurring as a result of excessive over-etching. Figure 4.15 shows an SEM image of the cross-section of a monitor sample after a 2 min He and O_2 etch in which the ARC has not been fully etched through but the PR on top of the ARC has been completely removed. A 4 min He and O_2 etch of the ARC layer on a monitor sample results in the pattern of holes being fully patterned into the ARC layer as shown in Fig. 4.16. Therefore, an etch time of 4 min was chosen for etching the 250 nm SOS resonant thermal emitter

ARC layer and the characterizations in the rest of this chapter occur after performing a 4 min ARC RIE. The ARC etch is performed using the NSL PlasmaTherm 790 Series RIE System and the specific etch parameters are given in Table A.5 in Appendix A. The same clean which is performed before the silicon dioxide inter-layer etch is also performed before the ARC etch, the parameters of which are also listed in Table A.5.
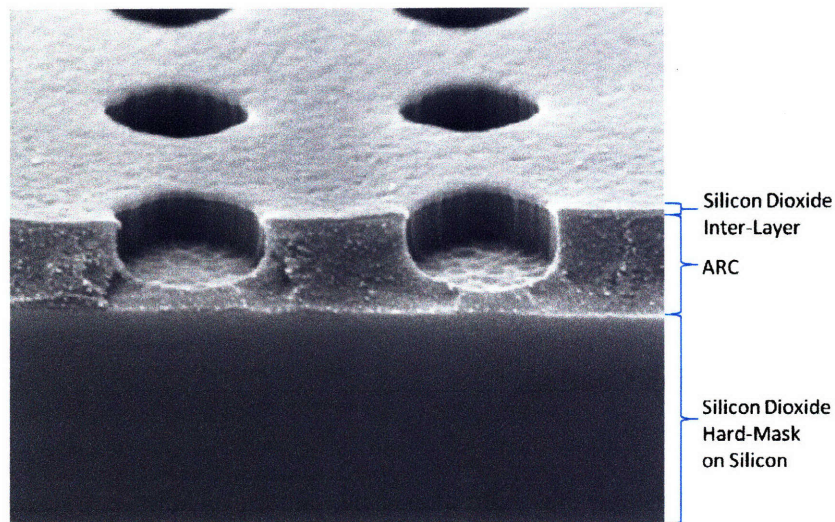
Figure 4.15: SEM image of the cross-section of a monitor sample after a 2 min RIE of the ARC layer in He and O_2. The holes have a periodicity of 1 μm.
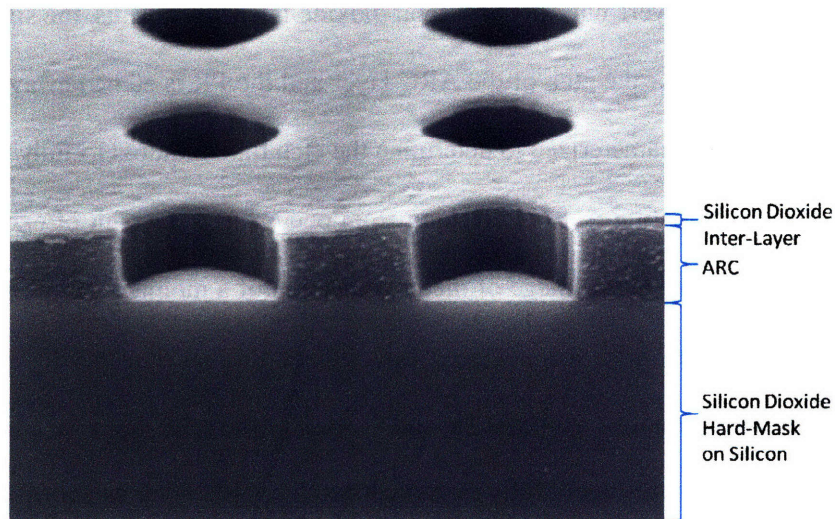
Figure 4.16: SEM image of the cross-section of a monitor sample after a 4 min RIE of the ARC layer in He and O_2. The holes have a periodicity of 1 μm.

4.3.3 RIE Silicon Dioxide Hard-Mask

The next step in the etching stage of the fabrication process of the SOS resonant thermal emitter is the transfer of the pattern of holes from the ARC layer into the silicon dioxide hard-mask layer, Fig. 4.12 (d). This step is known as the silicon dioxide hard-mask etch and is very similar to the silicon dioxide inter-layer etch due to the fact that the exact same RIE system with the same parameters is used for both. The difference between the two etches is the duration of the etch, the silicon dioxide hard-mask is 100 nm thick and so requires a longer etch time. The parameter of the silicon dioxide hard-mask etch and the chamber clean which is performed before each etch are listed in Table A.6 in Appendix A.

The etch gas used, CF_4, etches silicon dioxide, ARC and silicon so the silicon dioxide hard-mask etch must be characterized to determine the required etch time to fully etch through the silicon dioxide hard-mask without damaging the mask. Figure 4.17 shows an SEM image of the cross-section of a monitor sample after a 1 min: 30 s CF_4 etch in which the hard-mask has been etched through and some over-etching has occurred which has resulted in some of the silicon being etched. As expected the silicon dioxide inter-layer has been removed and some etching of the ARC layer has occurred. A shorter than 1 min: 30 s CF_4 etch might result in the silicon dioxide hard-mask not being etched fully whereas a longer etch could result in the ARC and silicon dioxide hard-mask being completely etched away. An etch time of 1 min: 30 s was chosen to etch through the 100 nm SOS resonant thermal emitter silicon dioxide hard-mask layer and the characterizations in the rest of this chapter occur after performing a 1 min: 30 s silicon dioxide hard-mask RIE. It must be noted that it is difficult to determine from an SEM images if the silicon

dioxide has been etched fully through as there is very little contrast between silicon dioxide and

silicon.
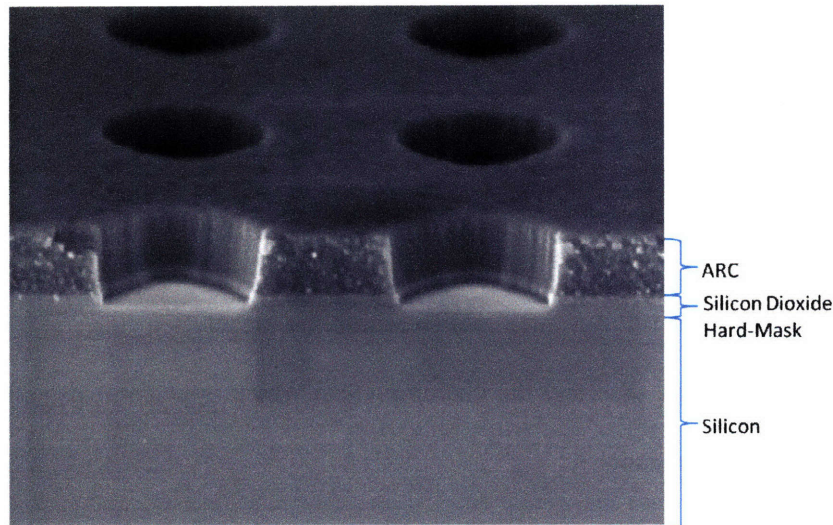
Figure 4.17: SEM image of the cross-section of a monitor sample after a 1 min: 30 s RIE of the silicon dioxide hard-mask in CF_4. The holes have a periodicity of 1 μm.

4.3.4   RIE Silicon and Silicon-on-Sapphire

The desired 2-dimensional photonic crystal SOS resonant thermal emitter is obtained by etching

the silicon dioxide hard-mask pattern into silicon using hydrogen bromide (HBr) gas in the Plas-

maTherm SLR-770 Series RIE System in the Space Nanostructures Laboratory (SNL), Fig. 4.12

(f). The removal of the ARC, Fig. 4.12 (e), and silicon dioxide hard-mask, Fig. 4.12 (g), are op-

tional. Nevertheless, as discussed below not removing the ARC causes problems with etching

silicon in HBr and not removing the silicon dioxide hard mask could alter the resonant thermal

emitter properties so it is recommended to remove both. The ARC removal step removes any

ARC which remains after the silicon dioxide hard-mask etch and is performed under the exact

same conditions as the ARC pattern transfer etch as described in Section 4.3.2 but the etch lasted 8 min instead of 4 min.

Every step in the fabrication process up until this point has been successfully characterized and implemented, Fig. 4.1 (a) – (g). However, major problems were encountered in the silicon etching step. It has been shown in [26] and [27] that silicon etching occurs in HBr with high selectivity to silicon dioxide. Although it must be pointed out that these results are based on different pre-processing steps and device geometries and so are not directly applicable. The choice of etch parameters was based on the results in [27], specifically the pressure and power setpoint were chosen to be 7 mT and 40 W respectively. Before each silicon etch the chamber was cleaned by a two stage cleaning process involving a 30 min plasma etch in oxygen followed by a 30 min reactive ion etch in oxygen. In order to coat the chamber a pre-deposition etch is performed, after the chamber clean, with the exact same parameters as the real etch but with no sample in the chamber. This passivation layer acts to protect the sample from contaminants from the chamber depositing on the substrate. The parameters for the two stage chamber clean and the silicon etch are given in Table A.7 in Appendix A.

Figure 4.18 shows two examples of unsatisfactory silicon etches. Figure 4.18 (a) is the result of an 8 min ARC removal step followed by a 30 min HBr RIE. It was believed that the undesirable trenching was due to a native oxide forming on top of the silicon in the holes during the ARC removal step. It is possible to remove native oxide in a CF_4 etch. Therefore, it was proposed to perform a short CF_4 RIE under the same parameters as described in Section 4.3.1 but for 15 s instead of 30 s. Figure 4.18 (b) shows the result of an 8 min ARC removal step followed by a 15 s CF_4 RIE and then a 30 min HBr RIE. No etching has occurred which suggests that it is not a na-

tive oxide on the surface of the holes in Fig. 4.18 (a). There are many possible causes which might have resulted in these two results and further research into the surface morphology of the sample before HBr RIE must be performed. One possible cause could be the silicon dioxide hard-mask. The process parameters on the PECVD system were often changed without the users knowledge and so the there is a possibility that the hard-mask is not high quality silicon dioxide. Another possibility is that due to the fact that there is extremely low contrast between silicon and silicon dioxide it is relatively impossible to determine if the silicon dioxide hard-mask has been fully etched through to silicon. It could also be possible that the specific ARC and native oxide removal techniques used actually damage the silicon in the holes. Therefore, it is proposed that research be performed into the use of EKC-265 manufactured by EKC Corp., California, USA, as an alternative to RIE for ARC removal. Also, it is possible to perform native oxide removal by immersing the sample in hydrofluoric (HF) acid for a short period of time and it would be worth investigating if this is superior to the short CF_4 etch which is currently used.

(a)   (b)
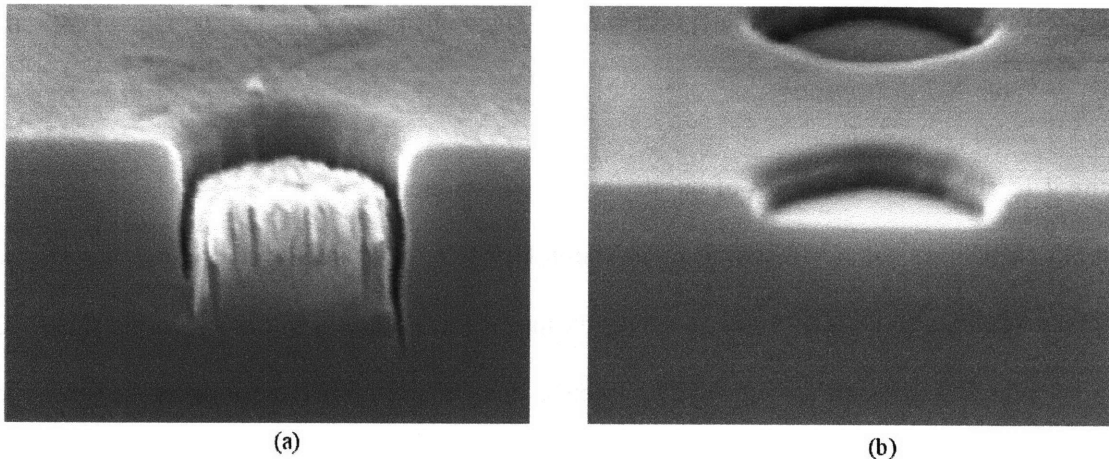
Figure 4.18: SEM images of the cross-section of two monitor samples after an 8 min ARC removal step, followed by (a) a 30 min HBr RIE, (b) a 15 s CF_4 RIE and then a 30 min HBr RIE. The holes have a diameter of 400 nm.

Chapter 5

Conclusion

This chapter summarizes the research which was conducted into the nanofabrication of a thermal emission device, specifically a 2-dimensional photonic crystal SOS resonant thermal emitter. The chapter begins with a description of the key points and results from each of the preceding chapters. Finally, recommendations are given of possible future research into the nanofabrication of a 2-dimensional photonic crystal SOS resonant thermal emitters.

5.1 Summary

This thesis presented an approach to the nanofabrication of a 2-dimensional photonic crystal SOS resonant thermal emitter. The motivation for this thesis and a review of related research was presented in Chapter 1. In Chapter 2, photonic crystals were introduced along with a description of two thermal emission devices which both use a very similar 2-dimensional photonic crystal structure. The two specific thermal emission devices were a resonant thermal emitter and a selective thermal emitter and the rest of the thesis focused on fabrication of the former.

Chapter 3 investigated the main technologies which were used in the fabrication of the 2-dimensional photonic crystal SOS resonant thermal emitter. It explained the processes which take place during deposition using PECVD and developed a model, from first principles, to be able to determine the thickness of a film after spin coating. Chapter 3 also discussed the theory behind

interference lithography, pattern formation in resist and specifically the Lloyd's mirror IL technique. A description of the function and operation of ARC and PR was also given. Finally, the process by which RIE occurs was explained.

Chapter 4 gave a description of the implementation, characterization and results of the fabrication of the 2-dimensional photonic crystal SOS resonant thermal emitter. The fabrication was divided into three major sections, specifically deposition, lithography and etching. The deposition stage involved the formation of the silicon dioxide hard-mask and inter-layer using PECVD and the spin coating of the ARC and PR layers, while the lithography stage involved the formation of the desired pattern of holes by use of Lloyd's mirror IL. The final fabrication stage, etching, dealt with the transfer of the pattern formed during the lithography stage into silicon. Throughout Chapter 4 the results of the characterizations which were performed at each stage in the fabrication process are presented and discussed. Out of the nine major steps in the fabrication of the SOS resonant thermal emitter, eight were successfully characterized and implemented but it was not possible to successfully characterize the RIE of silicon in HBr.

5.2   Future Work

The fabrication technologies and characterizations which were carried out in this thesis can be adapted to fabricate many other devices. Specifically, a 2-dimensional tungsten photonic crystal selective thermal emitter can be fabricated with minor adjustment of the 2-dimensional photonic crystal SOS resonant thermal emitter fabrication process. In terms of continued research into the SOS resonant thermal emitter the next immediate step would be to perform a more in depth cha-

racterization of the silicon etch step by attempting to use a slightly different mask stack or by using different pattern transfer techniques. Optical characterization could then be performed to compare the fabricated 2-dimensional SOS resonant thermal emitter structure with what is expected from theory. Also, research should be conducted into the ability to tune the frequency at which resonance occurs at a specific temperature by adjusting the period and radius of the holes in the 2-dimensional photonic crystal SOS resonant thermal emitter. The 2-dimensional SOS resonant thermal emitter has the potential to be used as a source and a sensor in the near-IR and IR regions of the spectrum but further research is required to verify it's applicability to these applications. Ideally it would be possible to create a narrow band thermal emitter which could be tuned to match the band-gap of a photovoltaic diode. This would offer exceptional efficiency in a TPV system.

Appendix A

	Silicon Dioxide Hard-Mask Deposition	Silicon Dioxide Inter-Layer Deposition
Gases	SiH4/N2/N20	SiH4/N2/N20
Flow Rate (sccm)	10/392/1420	10/392/1420
Pressure (mT)	900	900
Substrate Temperature (°C)	300	150
Showerhead Temperature (°C)	250	150
Power (W)	30	30
RF Generator Frequency (MHz)	13.56	13.56
Deposition Rate (nm/min)	46	46
Desired Thickness (nm)	100	20
Deposition Time (min:sec)	2:10	0:25

Table A.1: Silicon dioxide PECVD parameters.

	Refractive Index (325 nm)
Sapphire	1.80
Silicon	4.68 - 2.03i
Silicon Dioxide	1.48
BARLi ARC	1.55 - 0.14i
PS4 PR	1.681 - 0.016i

Table A.2: Refractive indices of materials, at 325 nm, for ARC thickness calculation [20].

	BARLi ARC	PS4 PR
Thickness (nm)	250	190
Spin Speed (rpm)	2000	3000
Softbake Temperature (°C)	175	90
Softbake Duration (s)	90	90
Post-Exposure Bake Temperature (°C)	-	110
Post-Exposure Bake Duration (s)	-	90
Developer	-	CD-26
Development Time (s)	-	60

Table A.3: BARLi ARC and PS4 PR spin coating, softbake, post-exposure and developement parameters.

Process	Chamber clean	Silicon Dioxide Inter-Layer Etch
Gases	CF4/O2	CF4
Flow Rate (sccm)	4.00/20.00	15.00
Pressure (mT)	20	10
Voltage Setpoint (V)	300	100
Desired Etch Depth (nm)	-	20
Etch Time (min:sec)	2:00	0:30

Table A.4: NSL PlasmaTherm 790 Series RIE System parameters for silicon dioxide inter-layer etch .

Process	Chamber clean	BARLi ARC Etch
Gases	CF4/O2	He/O2
Flow Rate (sccm)	4.00/20.00	10.00/5.00
Pressure (mT)	20	7
Voltage Setpoint (V)	300	250
Desired Etch Depth (nm)	-	250
Etch Time (min:sec)	2:00	4:00

Table A.5: NSL PlasmaTherm 790 Series RIE System parameters for BARLi ARC etch.

Process	Chamber Clean	Silicon Dioxide Hard-Mask Etch
Gases	CF4/O2	CF4
Flow Rate (sccm)	4.00/20.00	15.00
Pressure (mT)	20	10
Voltage Setpoint (V)	300	100
Desired Etch Depth (nm)	-	100
Etch Time (min:sec)	2:00	1:30

Table A.6: NSL PlasmaTherm 790 Series RIE System parameters for silicon dioxide hard-mask etch.

Process	Stage 1 Chamber Clean	Stage 2 Chamber Clean	Silicon Etch
Gases	O2	O2	HBr
Flow Rate (sccm)	20.00	20.00	20.00
Pressure (mT)	100	100	7
Power Setpoint (W)	300	300	40
RF Configuration	Plasma Etch	Reactive Ion Etch	Reactive Ion Etch
Desired Etch Depth (nm)	-	-	600
Etch Time (min:sec)	30:00	30:00	30:00

Table A.7: SNL PlasmaTherm SLR-770 Series RIE System parameters for silicon etch.

References

[1]   I. Celanovic, "Thermophotovoltaics: Shaping the Flow of Thermal Radiation," Ph.D. Thesis, Department of Electrical Engineering, MIT, May 2006.

[2]   D. L. Chan, I. Celanovic, J. D. Joannopoulos and M. Soljacic, "Emulating one-dimensional resonant Q-matching behavior in a two-dimensional system via Fano resonances," *Physical Review A*, vol. 74, p. 064901, December 2006.

[3]   N. Z. Jovanovic, "Microfabricated Thermophotovoltaic Selective Emitters," Ph.D. Proposal, Department of Electrical Engineering and Computer Science, MIT, June 2006.

[4]   L. Novotny and B. Hecht, *Principles of Nano-Optics*, Cambridge University Press, 2006.

[5]   John D. Joannopoulos, Robert D. Meade and Joshua N. Winn, *Photonic Crystals: Molding the Flow of Light*, Princeton University Press, 1995.

[6]   P. Vukusic and J. R. Sambles, "Photonic structures in biology," *Nature*, vol. 424, p. 852, August 2003.

[7]   H. H. Kolm, "Solar-battery power source," Quarterly Progress Report, Solid State Research, Group 35, MIT-Lincoln Laboratory, Lexington, MA, p. 13, May 1956.

[8]   P. Aigrain, "The Thermophotovoltaic Converter," unpublished lectures given at the Ecole Normale Superieure in 1956, and the Massachusetts Institute of Technology, Fall 1960 and Spring 1961.

[9]   K. Kwon, et al., "Additive oxygen effects in Cl_2 plasma etching of chrome films," *Journal of Materials Science Letters*, vol. 18, p. 1197, March 1999.

[10]   D. A. Glocker and S. I. Shah, *Handbook of Thin Film Process Technology*, Institute of Physics Publishing, 2002.

[11]   J. L. Vossen and W. Kern, *Thin Film Processes*, Academic Press, Inc., 1978.

[12]   A.G. Emslie, F.T. Bonner and L.G. Peck, "Flow of a Viscous Liquid on a Rotating Disk," *Journal of Applied Physics*, vol. 29, p. 858, May 1958.

[13]   D. Meyerhofer, "Characteristics of resist films produced by spinning," *Journal of Applied Physics*, vol. 49, p. 3994, July 1978.

[14]   S. Middleman and A.K. Hochberg, *Process Engineering Analysis in Semiconductor Device Fabrication*, McGraw-Hill, 1993.

[15]   D.W. Schubert and T. Dunkel, "Spin coating from a molecular point of view: its concentration regimes, influence of molar mass and distribution," *Material Research Innovations*, vol. 7, p. 314, October 2003.

[16]   M. E. Walsh, "Nanostructuring Magnetic Thin Films Using Interference Lithography," M.S. Thesis, Department of Electrical Engineering and Computer Science, MIT, August 2000.

[17]   S. N. Tandon, "Engineering Light Using Large Area Photonic Crystal Devices," Ph.D. Thesis, Department of Electrical Engineering, MIT, May 2005.

[18]   T. M. Shih, "Super-collimation in a Rod-based Photonic Crystal," M.S. Thesis, Department of Electrical Engineering and Computer Science, MIT, September 2007.

[19]   E. Hecht, *Optics*, Addison Wesley, Fourth Edition, 2002.

[20]   M. E. Walsh, "On the design of lithographic interferometers and their application," Ph.D. Thesis, Department of Electrical Engineering and Computer Science, MIT, September 2004.

[21]   H. Ito, "Chemical amplification resists: History and development within IBM," *IBM Journal of Research and Development*, vol. 41, p. 105, 1997.

[22]   R. A. Morgan, *Plasma Etching in Semiconductor Fabrication*, Elsevier, 1985.

[23]   J.D. Chapple-Sokol, W.A. Pliskin and R.A. Conti, "Energy Considerations in the Deposition of High Quality Plasma-enhanced CVD Silicon Dioxide," *Journal of The Electrochemical Society*, vol. 138, p. 3723, December 1991.

[24] H. Chatham, M. Mogaard, Yoshi Okuyama and H. Treichel, "Low Temperature Silicon Dioxide Deposition and Characterization," *Materials Research Society Symposium Proceedings*, vol. 913, symp. D03, p. 8, 2006.

[25] J.D. Chapple-Sokol, Carmen J. Giunta and R.G. Gordon, "A Kinetics Study of the Atmospheric Pressure CVD Reaction of Silane and Nitrous Oxide," *Journal of The Electrochemical Society*, vol. 136, p. 2993, October 1989.

[26] R. E. Barreto, "Fabrication of Optical Converters for Efficient Fiber-to-Silicon-Waveguide Couplers," M.S. Thesis, Department of Electrical Engineering and Computer Science, MIT, December 2006.

[27] S. Pendharkar, et al., "Reactive ion etching of silicon masks in the presence of an axial magnetic field," *Journal of Vacuum Science and Technology B*, vol. 13, p. 2588, November 1995.